For typeset version:

- Pieterek, B., Jones, T.J., 2025. Late Amazonian-aged volcanic cones of
- explosive origin in Ceraunius fossae, Tharsis, Mars. *Icarus*, 116870.
- 4 https://doi.org/10.1016/j.icarus.2025.116870

56

1

- 7 Late Amazonian-aged volcanic cones of explosive origin in Ceraunius
- 8 Fossae, Tharsis, Mars
- 9 Bartosz Pieterek^{1*}, Thomas J. Jones² and Chiedozie C. Ogbuagu^{3,4,5}
- 10 Geohazard Research Unit, Institute of Geology, Adam Mickiewicz University in Poznań; barpie@amu.edu.pl
- ² Lancaster Environment Centre, Lancaster University, Lancaster, UK; thomas.jones@lancaster.ac.uk
- 12 ³ Department of Earth, Ocean and Ecological Sciences, University of Liverpool, Liverpool, UK
- 13 ⁴ Department of Engineering and System Science, National Tsing Hua University, Hsinchu 30013, Taiwan
- ⁵ Department of Geology, University of Nigeria, Nsukka 410001, Enugu State, Nigeria
- *Corresponding author: barpie@amu.edu.pl

16 Abstract

17

18

19

20

21

22

23

2425

26

27

28

29

30

31

32

33

Detailed volcanological studies continue to enhance our understanding of Martian eruptive styles and their associated volcanic products. Growing evidence points to the involvement of mildly explosive eruptions as one of the eruption styles that contributed to the formation of distributed volcanic edifices in the volcanic province, Tharsis. This highlights a complex and dynamic eruptive evolution that occurred during the late Amazonian volcanism. Therefore, here, we report on the presence of smallscale, conical-shaped volcanic edifices located at the edge of Ceraunius Fossae in Tharsis. The association of the N-S aligned cones with a rough-surfaced lava flow enabled us to constrain the minimum age of their volcanic activity at ca. 48 Ma. Although they superficially resemble Martian scoria cones, their morphometric parameters indicate that they have a distinct and separate origin. They comprise coarser pyroclastic material such as spatter, and display an accumulation of likely volcanic bombs on the cones' slopes and at their bases, observable in the high-resolution images. Combining the sizes and distribution of the mapped individual volcanic bombs with a ballistic emplacement model enables us to calculate the exit velocity and maximum height for a given bomb density at a given launch angle. This provides a means to improve our understanding of ballistic trajectories and distances over which the pyroclastic material can be transported on Mars. Moreover, we argue that the portfolio of Martian volcanic edifices is more diverse than currently recognized. The use of high-resolution remotely sensed volcanological mapping could provide critical information about volcanic products and,

- 34 consequently, the magma fragmentation, which depends on the eruptivity, controlled by magma
- 35 composition and volatile contents.
- 36 **Keywords:** Mars surface, volcanism, geological processes, planetary dynamics, terrestrial planets

1. Introduction

Decades of Mars exploration, coupled with the continuous investigation of its surface through remotely sensed satellite imagery, provides new opportunities to research previously undocumented small-scale volcanic landforms. However, this progress also poses further questions and challenges (Mouginis-Mark et al., 2022). For example, recently, there has been a growing body of evidence suggesting that Amazonian volcanism might have been more differentiated than previously thought and may include numerous explosive-origin edifices (Brož et al., 2021; Flynn and Rader, 2024; Pieterek et al., 2024b; Pieterek and Jones, 2024). Although Tharsis hosts numerous conical edifices, some are morphologically unique, and their characteristics suggest formation through the accumulation of ballistically transported fragmented volcanic material (Brož et al., 2015, 2014; Flynn and Rader, 2024; Pieterek et al., 2024b; Pieterek and Jones, 2024), which has been interpreted to be scoria, spatter, or a combination of both. Such classifications are often supplemented by direct comparisons to terrestrial analogs and used to create and revise morphological classification schemes for conical edifices (Brož et al., 2014; Flynn and Rader, 2024; Pieterek et al., 2024a).

Although the Amazonian volcanic evolution of Tharsis was dominated by effusive eruptions that formed extensive volcanic regions (Crown and Ramsey, 2017; Hauber et al., 2009; Tanaka et al., 2014), there is evidence of (mild) explosive activity in some areas. This explosive volcanism can manifest on Mars' surface as small-scale volcanic features associated with summit vents of low shield volcanoes, individual edifices (e.g., pyroclastic cones, such as spatter or scoria), or local volcanic fields (Brož et al., 2021; Pieterek and Jones, 2024). However, due to the widespread occurrence of Amazonian effusive volcanism in Tharsis, some explosive-origin features could be buried under younger lava flows (Brož and Hauber, 2011). Consequently, our understanding of Martian volcanism is biased toward effusive eruptions that produce large-scale landforms. Despite this, satellite observations indicate that some of the explosive-origin features might have survived, either atop or close to the old, fractured terrains in Tharsis (Brož and Hauber, 2012a, 2011a; Pieterek et al., 2022b). The formation ages of explosive-origin features are constrained to span from the middle Amazonian for Ulysses Colles (Brož and Hauber, 2012) to the late Amazonian for Noctis Fossae (Pieterek et al., 2022b) and the late Amazonian spatter ramparts in Tharsis (Pieterek et al., 2024b; Pieterek and Jones, 2023). These relatively young ages (<100 Ma) determined for some of the explosive-origin features indicate that Mars retained, or still retains, the capacity for explosive activity, involving some degree of magma fragmentation through lava fountaining, which was possible during the late Amazonian period.

The occurrence of explosive-origin edifices has been inferred in most fractured terrains in Tharsis, including Ulysses Fossae, Noctis Fossae, and Claritas Fossae (Brož and Hauber, 2012; Pieterek et al., 2024a, 2022b). The only region that currently lacks a documentation of the presence of similar-looking volcanic features is located south of Alba Mons and associated with the Ceraunius Fossae (Fig. 1a). Therefore, to determine whether this region hosts similar volcanic features, we performed a dedicated

mapping campaign focused on identifying small-scale edifices in the southern region of Alba Mons. As a result, we mapped and investigated a previously unstudied cluster of small-scale, positive topographic landforms that are located at the transition zone between the Ceraunius Fossae terrain and late Amazonian lava flows. Our goal was to determine the geological origin and, if they are indeed of volcanic origin, provide insight into their eruptive behaviour. In this contribution, the term explosive refers to low- to moderate-intensity Strombolian and Hawaiian-style eruptions, during which the magma is fragmented and can construct scoria cones, spatter cones, or a combination of both through sustained or episodic lava fountaining, rather than high-intensity Plinian eruptions. This finding thus further supports the idea that explosive-origin landforms are more common in Tharsis than previously recognized, as they have often been overlooked (Pieterek and Jones, 2024). Moreover, the identification of the large pyroclasts that were ballistically emplaced offers a way to forensically uncover the eruption dynamics parameters that pertain to Martian explosive eruptions.

2. Geological setting

73

74

75

76

77

78

79

80

81

82

83

84

85

86

87

88

89

90

91

92

93

94

95

96

97

98

99

100

101

102

103

104

105

106

107

108

The largest volcanic province on Mars, Tharsis, is dominated by the widespread Hesperian-Amazonian age volcanic deposits (Tanaka et al., 2014) related to effusive eruptions (Bleacher et al., 2007; Pieterek et al., 2022a; Richardson et al., 2021), creating low shield volcanoes and associated lava flows (Flynn et al., 2022; Hauber et al., 2009; Wilson et al., 2009). These volcanic edifices are unevenly distributed throughout the Tharsis forming clusters of the youngest, late Amazonian-age volcanic fields adjacent to the major Tharsis volcanoes, Olympus Mons, Alba Mons, and the three volcanoes of Tharsis Montes (Pieterek et al., 2022a; Richardson et al., 2021; Tanaka et al., 2014). South of Alba Mons, in the Ceraunius Fossae region (Fig. 1a), topographically lower terrains are covered by extensive lava flows originating from low shield volcanoes whereas the adjacent highlands are comprised of highly fractured Hesperian age crust (Shahrzad et al., 2024; Tanaka et al., 2014). Specifically, Shahrzad et al. (2024) distinguished four main stages (see Fig. 14 in Shahrzad et al. (2024) of tectono-volcanic activity in Ceraunius Fossae occurring during the Amazonian period which are linked to magmatic diking centered beneath the region. With respect to the fractured terrains, the younger (late Amazonian) low shield volcanoes form spatially extensive edifices and are characterized by gentle slopes (<1-2°) (Hauber et al., 2009) indicating their construction by low viscosity lavas which are thought to be predominantly basaltic in composition (Hauber et al., 2011, 2009; Mangold et al., 2010; Peters et al., 2021). The alignment of the low shield volcano summit vents has a northward mean orientation (N008E) and is parallel to the adjacent crustal fractures, i.e., the fossae (Richardson et al., 2021). Therefore, low shield formation was most likely controlled by the migration of N-S trending radial dikes parallel to the regional extensional tectonic regime (Shahrzad et al., 2024) with a minor contribution of circumferential dikes related to the magma-plumbing system of Alba Mons (Pieterek et al., 2022a). In particular, the ages of the latest volcanic activity of distributed volcanism south of Alba Mons were established to range between 160 and 70 Ma (Hauber et al., 2011; Pieterek et al., 2022a). However, the youngest ages of distributed volcanic activity (~70 Ma) are geographically placed close to our region of interest (Hauber et al., 2011; Krishnan and Kumar, 2022; Pieterek et al., 2022a).

Here, our study region is situated south of Alba Mons (Fig. 1a) at the transition between the southern part of Ceraunius Fossae highlands and topographically lowered terrains covered by lava flows (Fig. 1b). Some of these lava flows are likely attributed to distributed volcanism (Pieterek et al., 2022); nevertheless, one flow is associated with the studied features and enabled the determination of their formation age (Fig. 1b-c). The contact between these two structural units is highlighted by a >100-meter high scarp (Fig. 1b-c). The background topography of the volcanic lowlands gradually decreases in elevation from the east to the west, however, it is punctuated by local volcanic vents.

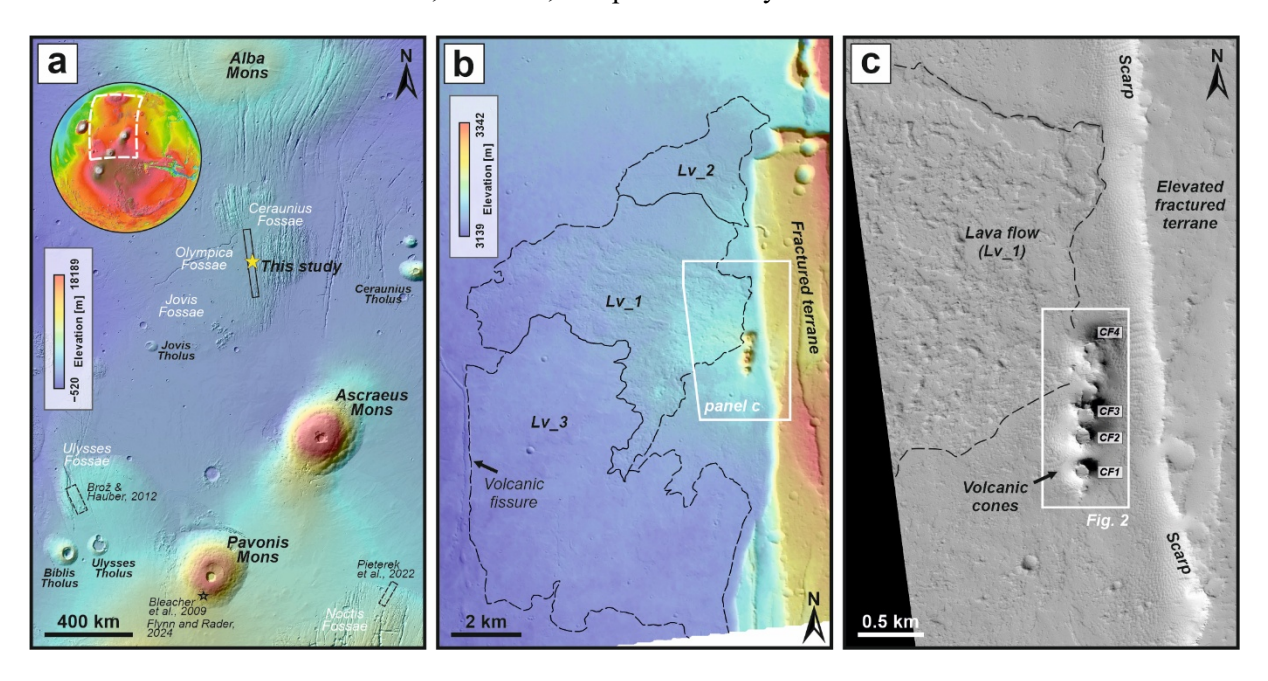


Fig. 1 (a) The top left inset shows the Mars Orbiter Laser Altimeter (MOLA) topographic map of Mars with the white rectangle indicating the area shown in panel (a). An overview map of the central part of Tharsis volcanic province with the marked location of the studied region. The locations of two volcanic fields of scoria cones in Tharsis (Brož and Hauber, 2012; Pieterek et al., 2022b) are marked by dashed black rectangles. The basemap is produced using the MOLA shaded relief basemap (463 m/px) overlaid by MOLA- High Resolution Stereo Camera (HRSC) digital elevation model (DEM) (Fergason et al., 2018). **(b)** A colour image of the region of interest, generated from the Context Camera-based (CTX) DEM (derived from the stereo-pair F10_039645_2056 and F11_040001_2056, centered at 25.63°N and 250.25°E, with a spatial resolution of 12 m/px), illustrates the studied features located close to the scarp separating the western lowlands comprised of late Amazonian lava flows and Hesperian-age fractured highlands. The black dashed line marks the outer margin of the mapped flow-like unit associated with the studied cones. **(c)** The High Resolution Imaging Science Experiment (HiRISE) image (ESP_057051_2050, centered at 24.667°N and 250.399°E) presenting the studied features. The black dashed line again marks the edge of the flow unit, as in the previous panel.

3. Methods

3.1. Mapping and datasets used

To investigate the topographical features presented in this contribution, we used satellite images from the Context Camera (CTX: ~5 m/px) (Malin et al., 2007) and the High Resolution Imaging Science Experiment (HiRISE: ~50 cm/px) (McEwen et al., 2007) both carried onboard the Mars Reconnaissance

Orbiter (Table 1). The initial mapping was conducted based on the global CTX mosaic (Dickson et al., 2024) which was further supplemented by individual CTX and HiRISE images downloaded from the NASA Planetary Data System (Table 1). Although the CTX mosaic offers a seamless, global view of the planet, its data quality is partially lost due to blending and stitching, whereas individual images, through preserving subtle brightness variations, enable more precise analysis of small-scale features and surface details. Therefore, the CTX images with a sufficient resolution of 5–6 m/pixel are commonly used to determine the geological context and to study the small-scale volcanic features (Edgett, 2009; Hauber et al., 2009). The presence of overlapping CTX images enabled us to produce stereo-pair-based digital elevation models (DEMs) using the dedicated data processing information system called MarsSI (Mars System of Information) (Quantin-Nataf et al., 2018). The produced DEMs has a surface scale of ~12 m/pixel and a vertical resolution of ~4 m allowing us to conduct precise topographic measurements (Table 1). These CTX-based DEMs, derived from MarsSI, were used for topographic analyses, including slope measurements and volume calculations of the studied cones.

137

138

139

140

141

142

143

144

145

146

147

148149

150

151

152

153

154

155156

157

158

159

160

161

162

163

164

165

166

167168

169170

171

Going forward, we abbreviate the individual cones as CF followed by the subsequent number of the cone. The cone boundaries were determined using CTX-based topographic profiles, which allowed us to define the break in slope relative to the surrounding terrain. These boundaries were then mapped using the CTX DEM-derived slope map and the corresponding HiRISE image (to supplement the surface texture observations). Due to the coarse resolution of the CTX DEM, we define the base of the cone as the point where the slope exceeds approximately 3–4° (Fig. S1), since the surrounding terrain typically exhibits slope values of up to 2°. This approach also allowed us to calculate cone heights and approximate slope values along the W-E axes of the cones using trigonometry. To verify these measurements, we used CTX DEM-derived slope map to calculate average slope values along the same W-E axes (Fig. S1b). For this, we extracted slope values by applying masks that cover the area from the base to the summit crater rim (Fig. 1b) and analyzed the resulting statistics. Using the generated W-E profiles, we demonstrated that the coarse resolution of the CTX DEM did not allow us to clearly define the summit craters (Fig. S2). Therefore, we estimated the cone volumes using the simplified cone equation; volume = basal area multiplied by cone height, where the basal area is assumed to be a circle with the average diameter of the cone. The mapped flow-like unit boundaries (Lv 1, Lv 2, and Lv 3; Fig. 1b) were determined by tracking greyscale variations within the CTX image and identifying difference in surface texture (Fig. 1). Additionally, mapping was supplemented by analysis of topographical profiles derived from CTX DEMs, which allowed us to identify the lava flow bases. To provide a more detailed morphological description of the cones and associated surface features (i.e., the spatial distribution of pyroclasts), we used the HiRISE image (ESP 057051 2050), which has a mapprojected scale of 50 cm/pixel (Table 1). All image and data analysis associated with mapping was conducted using ArcGIS software ArcMap and ArcScene version 10.5.

Table 1. Details of the Context Camera (CTX) stereo-pair images and High Resolution Imaging Science Experiment (HiRISE) image used for this study. Dates are given in the format year-month-day.

Image ID	Imagery system	Center Latitude	Center Longitude	Scaled pixel grid	Acquisition date	Subsolar azimuth	Incidence angle
P12_005875_2042	CTX	24.26°	250.60°	5.66 m	2007-10-28	144.08°	45.89°
P06_003396_2048	CTX	24.85°	250.25°	5.65 m	2007-04-18	153.42°	65.48°
F10_039645_2056	CTX	25.63°	250.28°	5.88 m	2015-01-10	139.41°	65.99°
F11_040001_2056	CTX	25.63°	250.25°	5.69 m	2015-02-07	136.36°	61.65°
J09_048216_2047	CTX	24.79°	250.18°	5.67 m	2016-11-08	138.93°	63.50°
ESP_057051_2050	HiRISE	24.6677°	250.4035°	0.50 m*	2018-09-27	132.8357°	63.3013°

*HiRISE resolution is given for map-projected images.

3.2. Age determinations

172173

174

175

176177

178

179

180

181

182

183184

185

186

187

188

189

190

191

192

193

194

195

196

197

198

Spatiotemporal volcanic reconstructions often require absolute dating which is challenging for smallscale features on Mars. Although the studied cones are too small for reliable crater-counting dating, the surrounding and underlying volcanic units, which resemble lava flows (Lv 1, Lv 2, and Lv 3; Fig. 1b) and are spatially related to the cones, are large enough for their formation ages to be determined. This, in turn, allows us to establish the maximum possible age of the cones. Relative structural relationships between the units was established using imagery and the corresponding DEM and allowed us to assess the consistency between the absolute ages and stratigraphic order. Here, we dated three flow-like units (Fig. 1b) adjacent to the studied cones, with surface areas ranging from 6.7 to 44.4 km². These units host between 26 and 366 impact craters, from which the number of impact craters were specifically used for fitting Crater Size-Frequency Distributions (CSFDs) varies from 14 to 38. The age of each volcanic unit was determined using the crater counting methods and utilizing the mapped craters with diameters >35 m (the exact minimum craters diameter used varies depending on the randomness analysis results). Such a small range of minimal crater diameters has already been used for fitting the isochron on other volcanic terrains based on the CTX images (Brož et al., 2017b; Golder et al., 2020; Hauber et al., 2011; Pieterek and Jones, 2023). The crater mapping and CSFD plots were performed by applying the ArcGIS plug-in, CraterTools2.1 (Kneissl et al., 2011). Crater statistics and derivation of crater model ages, including their errors, were carried out using the CraterStats II software (Michael and Neukum, 2010). In this contribution, we used ages based on the Hartmann (2005) chronology model and the Poisson timing analysis, which allowed us to avoid any bias related to the binning of crater size (Michael et al., 2016). Other chronology systems were also used to calculate the unit ages for reference to other studies. The set of minimum craters diameter used for fitting isochron was based on the results of the randomness analysis (Michael et al., 2012), which defines the degree of clustering to evaluate the potential contamination of secondary craters. The shapefiles including dated areas, mapped impact craters, and CraterStats files for all dated volcanic terrains can be found in an online, external repository (Pieterek et al., 2025).

3.3. Bomb measurements

HiRISE image observations reveal that some parts of the flanks of the studied cones host rocks that resemble pyroclasts and are distributed radially to eruption centre (Table S1). Specifically, they are located both on the slopes and at the base of the cones. We note that the measured diameters represent minimum estimates, as continued explosive activity could partially bury earlier emplaced pyroclasts or their fragments. While partial burial may obscure full dimensions, our analysis assumes that the visible portion reflects the largest exposed cross-section limited by the image resolution and therefore provides a conservative estimate of size. We interpret these features to be volcanic pyroclasts (specifically, terrestrial volcanic bombs or blocks, as >64 cm in diameter) that were ballistically emplaced. We fully justify this interpretation in discussion Section 5.1. Specifically, here, we investigated the spatial distribution and size of the bombs associated with the CF2 cone (Fig. 2). The shapes of the CF3 and CF4 cones have likely been modified, making it impossible to determine their ejection centers. Additionally, the northern slope of the CF1 cone overlaps with the CF2 cone, and observable bombs in this area may be mixed between the two cones.

The position of the CF2 bombs (Fig. 2a) was mapped using the ArcMap 10.5 software and their size (maximum observable diameter) was manually measured. Given the HiRISE resolution of 55.7 cm/pixel, the bombs of diameter exceeding ~1.5 meters (3 by 3 pixels) could be confidently recognized. Although smaller features could be classified as bombs, we have not included them in our considerations. To provide spatial characteristics, we measured the lateral distance in plan view between the center point located inside the summit vent which has an elevation of 3296 meters, and the location of the bomb (Fig. 2b). For each bomb mapped as a point, we determined the elevation at its location using the ArcGIS Extract Values to Points tool applied to the corresponding CTX-based DEM. Due to the coarser resolution of the CTX-based DEM with respect to the HiRISE image used for mapping, we enabled an optional parameter in the ArcGIS Extract Values to Points tool. This allowed the elevation at each bomb location to be calculated using a bilinear interpolation between the adjacent cells with valid values. Using the obtained elevation values, we calculated the height difference between the bomb and the summit vent. Moreover, in plan view, we determined the angle between the northern reference line and the line between the center of the summit vent and the bomb (Fig. 2b). All these values were calculated using the ArcMap-based Field Calculator tool for determining the incidence angle of a polyline.

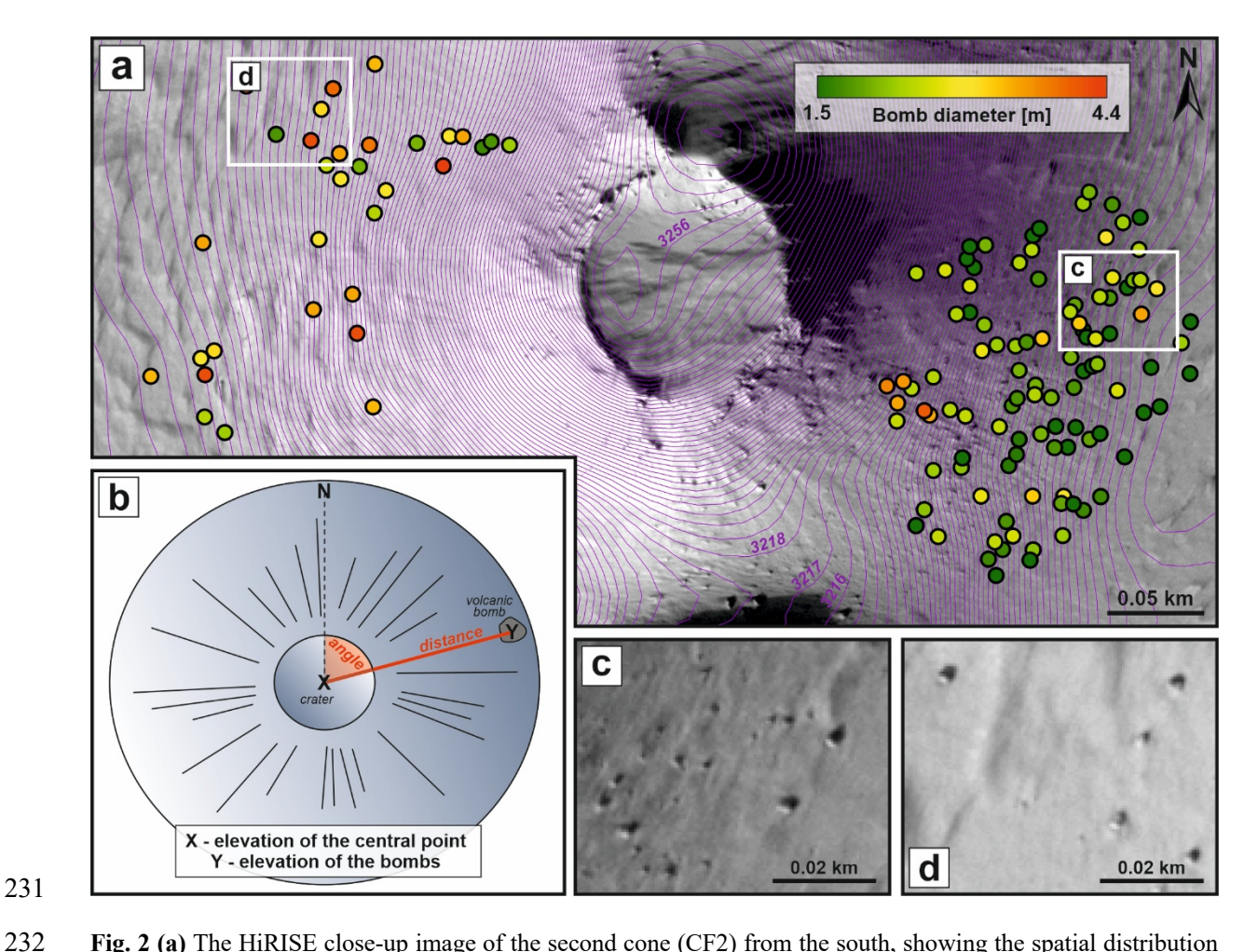


Fig. 2 (a) The HiRISE close-up image of the second cone (CF2) from the south, showing the spatial distribution of the mapped volcanic bombs. The color scale indicates increasing volcanic bomb size. Purple contour lines, separated at 1-meter intervals, are derived from the CTX DEM (stereo pair F10_039645_2056 and F11_040001_2056). (b) Schematic illustration presenting the methodology applied to the characterization of the mapped bombs. (c-d) The zoom-in HiRISE images from two different flanks of the CF2 showing the identified bombs. Note that larger bombs are accompanied by smaller fragments that fall below our confident recognition limit of \sim 1.5 m diameter.

3.4. Ballistic modelling

We conducted numerical modelling under the assumption that the majority of the identified rocks on the CF2 cone flanks are in fact volcanic pyroclasts – i.e., bombs that were ballistically emplaced during the eruption. Their sizes and spatial distribution were used to calculate eruption parameters specific to the analyzed cone. We used the Runge Kutta method to resolve the ballistic trajectory of a pyroclast, travelling through air, from a vent at a given exit velocity, w and launch angle, θ . The model considers the variables along the flight path to form a series of equations that provide the range (i.e., the horizontal distance from the vent) reached, flight time, velocities and height attained during flight. The equations for our model were derived from sections 1.2, 1.4 and 1.5 of (Biringen and Chow, 2011) and were further reproduced from Ogbuagu et al. (2025). For completeness aspects of the Ogbuagu et al. (2025) model are reproduced here and the modifications made to account for Martian surface conditions, but for further modelling details the reader is referred to Ogbuagu et al. (2025). Assuming a non-rotating and spherical pyroclast, we described the motion of a rigid body under the action of a system of forces

in a two-dimensional (2-D) Cartesian system (x, y). These forces include the buoyant force $= m_f g$, which accounts for weight of the fluid displaced by the moving spherical body during ascent. Here, $m_f = 1/6\pi d^3 \rho_f$, where m_f and ρ_f are mass and density of the surrounding fluid, respectively and g, acceleration due to gravity is taken as 3.71 m s⁻². Also, the weight of the body that pulls it down as it ascends = -mg. An accelerating body going through an active fluid experiences added mass. This added mass, for spherical bodies, is half of the fluid mass displaced by the body (Pantaleone and Messer, 2011) and the associated force of motion is defined as,

$$\frac{1}{2}m_f\frac{dv}{dt} \tag{1}$$

The drag force, influenced by the particle Reynolds number as it travels through the fluid medium is also considered and given by

$$\frac{\pi}{8}\rho_f v |v| d^2 C_d(v) \tag{2}$$

where C_d is the drag coefficient for the spherical body and d is the diameter. An absolute velocity, |v|, was used for the viscous drag instead of v^2 because the drag may be in an opposite direction to the

263 pyroclast velocity, v. Summing these forces gives,

$$m\frac{dv}{dt} = -mg + m_f g + \frac{1}{2}m_f \frac{dv}{dt} + \frac{\pi}{8}\rho_f v |v| d^2 C_d(v)$$
 (3)

264 And rearranging Eq. (3) gives,

$$(m - \frac{1}{2}m_f)\frac{dv}{dt} = -(m - m_f)g + \frac{\pi}{8}\rho_f v|v|d^2C_d(v)$$
(4)

For a spherical bomb launched at an angle, θ , from the horizontal (x-axis), and with exit velocity, \mathbf{w} , which has u and v components, into moving/active air medium with velocity, w_f , which also has u_f

and v_f components, the resultant force, f, acting on the body can be determined by the relative velocity

of the air/gas to that of the body, $w_r = w_f - w$. This resultant force also has f_x and f_y components,

which are expressed as:

267

$$f_x = |f| \cos \theta = \frac{\pi}{8} \rho_f d^2 C_d (u_f - u) w_r \tag{5}$$

$$f_y = |f| \sin \theta = \frac{\pi}{8} \rho_f d^2 C_d (v_f - v) w_r \tag{6}$$

270 Considering the vector components (f_x and f_y), Eq. 4 is then represented as

$$\left(m - \frac{1}{2}m_f\right)\frac{d^2x}{dt^2} = f_x \tag{7}$$

$$\left(m - \frac{1}{2}m_f\right)\frac{d^2y}{dt^2} = -(m - m_f)g + f_y$$
(8)

where f is a function of position (x and y), velocity (u and v), and time (t),

$$\frac{dx}{dt} = u; \frac{du}{dt} = f_x(x, y, u, v, t)$$
(9)

$$\frac{dy}{dt} = v; \frac{dv}{dt} = f_y(x, y, u, v, t). \tag{10}$$

- Expressing m and $m_f/2$ in terms of densities, ρ and ρ_f , and substituting f_x , f_y with Equations (5) and
- 273 (6) above, Equations (7) and (8) after rearrangement can be re-written as,

$$\frac{d^2x}{dt^2} = \frac{3\bar{\rho}}{4d} C_d (u_f - u) w_r / (1 - \frac{1}{2}\bar{\rho})$$
 (11)

$$\frac{d^2y}{dt^2} = \left[-(1-\bar{\rho})g + \frac{3\bar{\rho}}{4d}C_d(v_f - v)w_r \right] / (1-\frac{1}{2}\bar{\rho})$$
(12)

where $\bar{\rho} = \rho_f/\rho$ and w_r is the relative velocity $(=\sqrt{(u_f - u)^2 + (v_f - v)^2})$.

275

276

277

278

279280

281

282

283

284

Here, the model inputs are the background air velocity (u_f or v_f), fluid density (ρ_f), fluid viscosity μ_f , pyroclast exit speed (w), exit/launch angle (θ), minimum pyroclast diameter (d), and the pyroclast density (ρ). For our calculations, we adopted the density, ρ_f and dynamic viscosity, μ_f of the Martian air to be 0.02 kg m⁻³ (Bridges et al., 2010; Rowland et al., 2004) and 1.3 × 10⁻⁵ Pa s (Almeida et al., 2008; Edgett and Christensen, 1991; Petrosyan et al., 2011), respectively, and set the background air velocity to be zero (i.e., no atmospheric wind). To ensure solution stability while using the Runge Jutta method solver (Carnahan et al., 1969), small step sizes of 0.1 s and 1 m were adopted for the time and position spacings, respectively (Fig. S3). This method, using Equations 1 through 12, was applied assuming a constant drag coefficient, $C_d = 0.7$, and the same data input, to validate the model of Ogbuagu et al. (2025) against the previous work of Brož et al. (2014).

Then, to improve on the constant drag coefficient assumption (Brož et al., 2014), here, we also compute the ballistic trajectories for the more realistic condition where C_d is dependent on the particle Reynolds number (Re):

$$Re = \rho_f |v| d/\mu_f \tag{13}$$

and then we assigned C_d based on the experimental curve for Re vs C_d for smooth spheres by (Goldstein, 1938). Where:

$$C_d = 0 for Re = 0 (14)$$

$$C_d = 24/\text{Re} \qquad \text{for Re} > 0 \le 1 \tag{15}$$

$$C_d = 24/\text{Re}^{0.646}$$
 for $\text{Re} > 1 \le 400$ (16)

$$C_d = 0.5$$
 for Re > $400 \le 3 \times 10^5$ (17)

$$C_d = 0.000366 \times \text{Re}^{0.4275}$$
 for Re > 3 × 10⁵ ≤ 2 × 10⁶ (18)

$$C_d = 0.18$$
 for Re > 2 × 10⁶ (19)

This variable drag coefficient approach was used for all calculations related to the volcanic bombs identified in this study.

Using the bomb position observed in the remotely sensed dataset, we can quantify the exit velocity for all volcanic bombs for a given clast density and a given launch angle. For small Martian pyroclasts of 4 cm in size, (Brož et al., 2014) used a density of 850 kg/m³. However, on Earth the density has been observed to vary between 950 and 2900 kg/m³ (Bombrun et al., 2015) for bombs and pyroclasts <4 m in diameter (Taddeucci et al., 2017). The density of the bombs of the most similar size (0.07–4.59 m) produced during the Stromboli eruption in 2010 to our mapped rocks range from 1370 to 2300 kg/m³ (Gurioli et al., 2013). Therefore, supported by previous ballistic modelling of volcanic bombs, on both Earth and Mars, here, we varied the bomb density between 1500 and 2700 kg/m³. Guided by the dataset of (Vanderkluysen et al., 2012), and excluding bombs that experienced an in-flight collision and one with a launch angle of 90°, the launch angle was varied between 37.0° and 89.0°, with a mean of 81.8°.

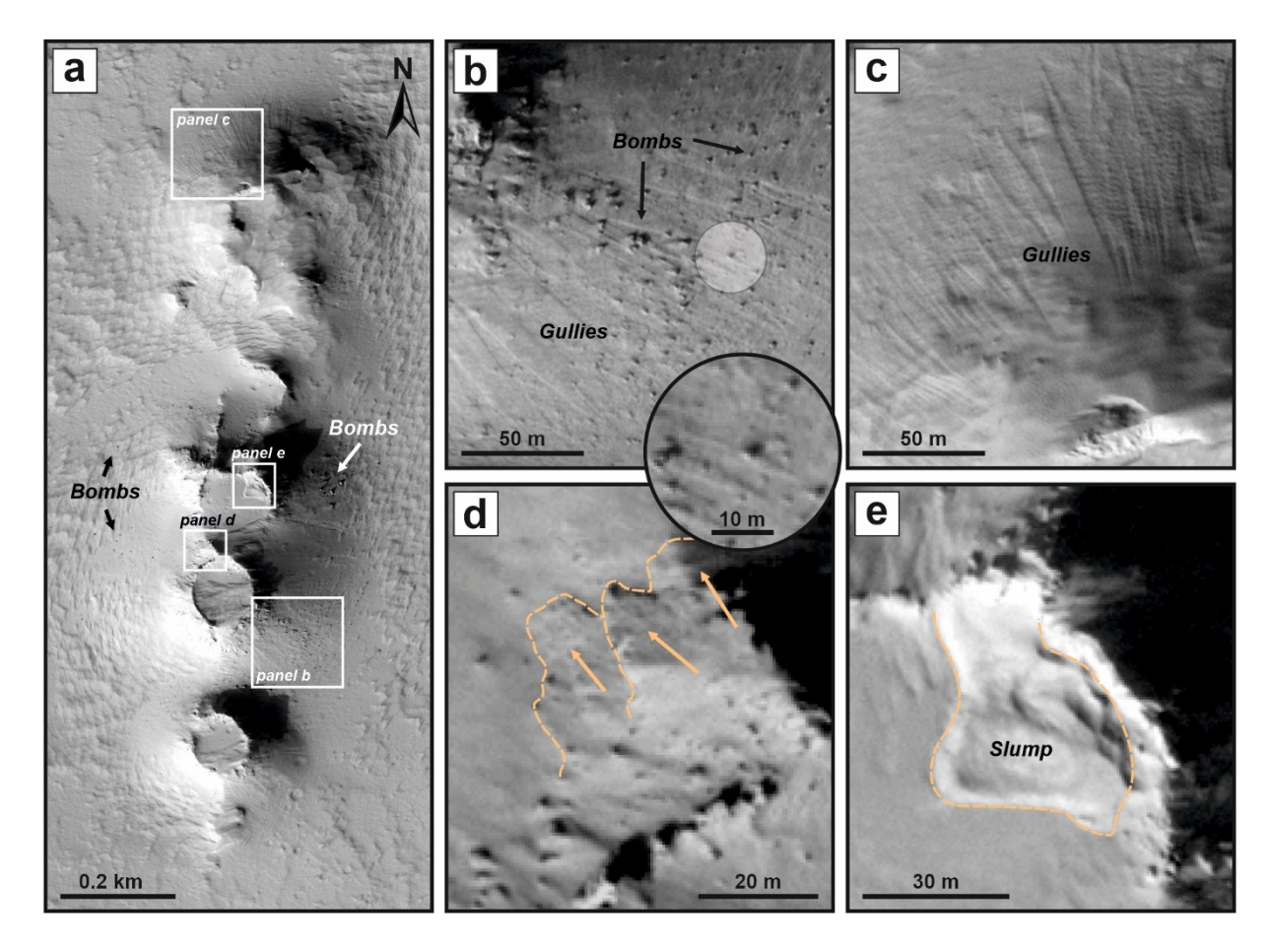


Fig. 3 (a) Part of HiRISE camera image (ESP_057051_2050) illustrating the morphology of the studied cones (CF1 through CF4). The white rectangles mark the locations of regions of interest displayed in other subpanels. **(b)** Close-up image of the southeastern slope of CF2 shows the radially distributed pyroclasts, interpreted as volcanic bombs, and linear V-shape structures on the slope. **(c)** Example of the V-shape linear structures developed on the northern slope of CF4. **(d)** Close-up image of the summit crater rim and northwestern slope of the cone that have a rough and knobby texture. **(e)** Structure developed on the flank of the most complex and modified edifice (CF3) possibly related to a large mass movement event (i.e., collpase) or slumping processes.

4. Results

4.1. Morphology and age

The four identified edifices (CF1 through 4) are aligned in a N-S (N010E) direction parallel to the adjacent scarp separating the late Amazonian volcanic terrains and the Hesperian fractured crust of Ceraunius Fossae (Fig. 3a). They form a 1.4 km long ridge comprising at least four individual edifices (Fig. 3a). Two southernmost edifices (CF1 & 2) have circular shapes with well-developed summit craters, whereas two northern edifices (CF3 & 4) are characterized by irregular shapes without well-defined craters. At the southern flank of CF1, an elevated structure is present which follows the cone's N-S orientation and could be formed by either a cone fragment rafted away by lava flows during the early construction of CF1, or is another early eruption location, later buried by CF1 deposits. The conical edifices are also accompanied by volcanic bombs of varied sizes (Figs. 2 and 3b), occurring both on the slopes and at the base of the edifices. Moreover, some parts of the edifice flanks reveal the presence of V-shape structures (Fig. 3c), expanding in width towards the base of the cones. There is no clear

relationship between these structures and the presence of the bombs, thus we suggest that they are not related in origin. Although the cones and surrounding area are covered by fine-grained material, the rocks outcropping mostly at the summit crater rims show a rough and knobby texture and comprise short, lobate features (Fig. 3d). In addition, the most morphologically complex edifice, CF3, exhibits the presence of a slump-like feature with a smooth surface extending downslope from the plausible summit crater rim (Fig. 3e). In addition, CF3 is characterized by a gentle curved depression that breaks the western slopes (Fig. 3a). The area to the west of the cones is covered by a rough flow-like unit, interpreted to be a lava flow (Fig. 1c) which originates from the cones and is up to 6.5 km in length. In plan view, this unit has irregular, lobate-shape outlines (Fig. 1b) and flow direction follows the regional topography. The boundary to the surrounding relatively smooth surface terrain can be clearly identified on the CTX-based DTM and shows that the lavas have a thickness of <10 m.

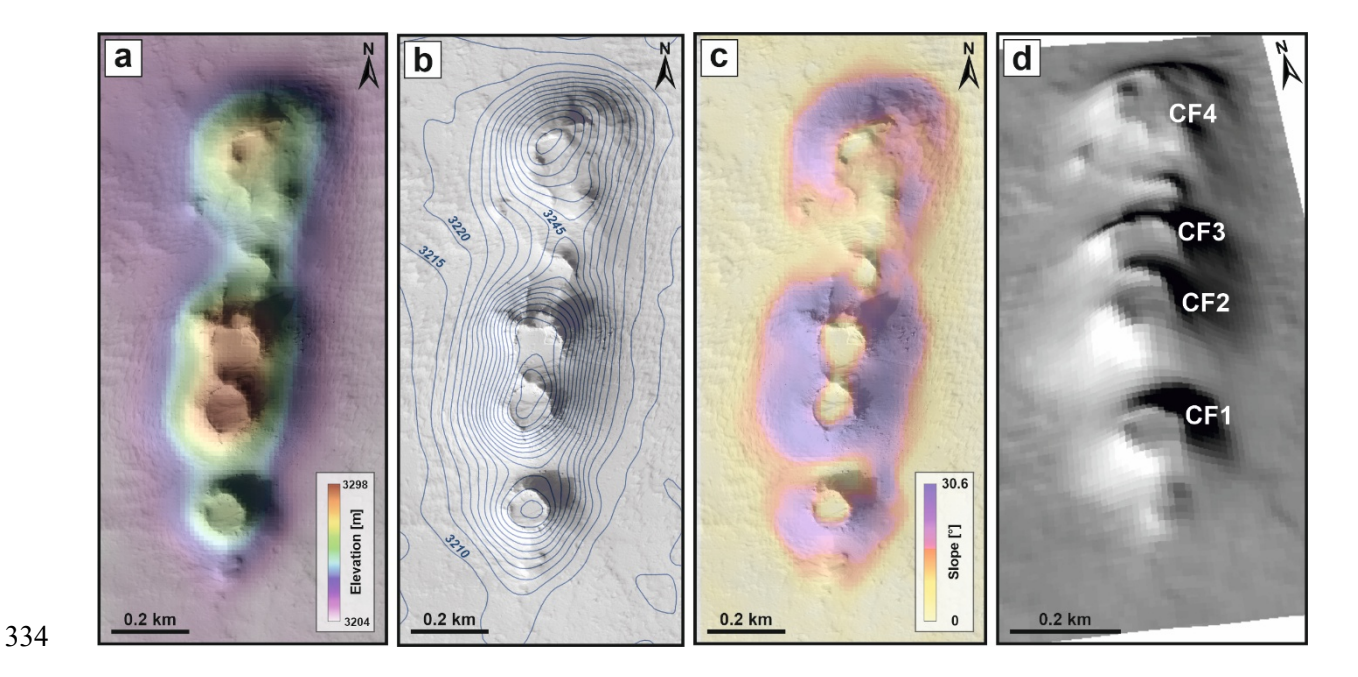


Fig. 4 (a) The CTX-based digital elevation model of the studied cones superimposed on top of the HiRISE image. The CTX stereo-pair comprises F10_039645_2056 and F11_040001_2056 images, centered at 25.63°N and 250.25°E. The following panels constitute the product maps based on the DEM and include **(b)** a contour map, **(c)** a slope map, and **(d)** a 3D visualization of the cones which is vertically exaggerated two times.

The two best-preserved edifices (CF1 & 2) occur as highly conical structures with large summit craters. The long axes of the summit craters (N-S), which are aligned parallel to the cone alignment, measure 106 m and 124 m, respectively, while the perpendicular axes measure 101 m and 108 m, respectively (Fig. 3a). The mean values calculated based on 4 radially constructed axes are 100 m and 112 m, respectively. Determining the width of each cone base is challenging due to the overlapping boundaries of each edifice, especially of their N-S flanks. Using the W-E topographical profiles derived from the CTX DEM and supplemented by HiRISE image observation, we determined the width of the CF1 and CF2 cones to be ~465 and ~620 m, respectively. This results in the crater width to cone width ratios of 0.22 and 0.20. Based on the CTX-based DEM topographical profiles along W-E axes, the cones

are on average 51 m (CF1) and 87 m (CF2) high (measured on both sides of each cone), which, using trigonometry, yields average slopes of 12.7° and 16.3° (Fig. 4b-c). Using the same W-E axes, the ArcMap statistics yielded average slope values of 14.8° (CF1) and 17.1° (CF2) for the defined areas (Fig. S1). Unlike the trigonometry-based calculations, this method accounts for the entire slope surface within the considered area. Using the estimated elevation of the base of the cones, we calculated their volumes to be $1.15 \times 10^{-2} \, \mathrm{km^3}$ and $3.50 \times 10^{-2} \, \mathrm{km^3}$, again for CF1 and CF2, respectively. Based on image observations and the corresponding DEM, we infer that the northern cones (CF3 & 4) have similar morphology to the southern ones. This is supported by the DEM-based topographical and slope maps, as well as 3D visualization (Fig. 4d). The northern flank of CF3 and southern flank of CF4 show signs of deformation, including lava outflow, structures resembling rafted mounds, and mass-wasting slumps (Fig. 3), whereas the other cones (CF1 & 2) retain a semi-conical shape.

Table 2. The ages obtained by the surface crater dating of the lava flow units (Lv). The age of Lv_1 represents the maximum age of the explosive-origin cones identified.

Volcanic unit		Lv_1		L	v_2	Lv_3		
Area [km²]		27.6		44.4		6.7		
Number of mapped craters		54		365		26		
Number of craters used for fitting		37		38		14		
Min. size of craters [m]		35		50		40		
Max. size of craters [m]		150		200		1	130	
Chronolog y systems	Neukum-Ivanov, 2001	26.2	±4.3	51.7	± 8.3	66.5	+19.0; -16.0	
	Ivanov, 2001	30.9	±5.1	61.1	±9.9	78.5	+22.0; -19.0	
	Hartmann, 2005	48.0	±7.9	85.5	± 14.0	117	+33.0; -28.0	

 \pm is 1σ as age uncertainty based on the number of craters fitted.

Remote-sensed mapping of the terrains surrounding the cones revealed the presence of lava flows (Fig. 5a), which enable temporal constraints on the volcanic activity in this field. Specifically, the spatial association between the studied cones and the western flow unit (Lv_1) coupled with the age dating, allowed us to constrain the possible age of cone formation (Table 2). The impact crater distribution (Fig. 5a) shows that the proximal parts of Lv_1 lack evidence for the presence of craters, and as such the proximal to distal distribution of craters on the lava surface is heterogenous. Despite this general observation, the randomness analysis results fall within the acceptable range of values for reliable age determination (see Section 3.2). The stratigraphically uppermost unit spreading from the cones yields a model age of 48 ± 8 Ma with 37 craters used for isochron fitting (Fig. 5b and Table 2). To supplement this result, we dated adjacent terrains (Lv_2 and Lv_3) that underlie, and thus likely predate, Lv_1. The flow unit associated with N-S-trending fissure (Lv_3) shows an age of 85 ± 10 Ma. In addition, on top of the elevated, fractured terrane of Ceraunius Fossae, we identified two NNE-SSW aligned depressions, resembling either volcanic vents or pits, which are common in this region (Shahrzad et al., 2024). One of these depressions is associated with an outlet channel that breached the scarp and generated a short

flow unit (Lv_2) dated as 120 ± 30 Ma. The semi-circular shape of the depression, its NNE-SSW elongation, the associated flow unit with surface texture similar to Lv_1, and the broader geological context supports its interpretation as a plausible volcanic vent. The ages of these two units (Lv_2 and Lv_3) overlap each other within error (Table 2).

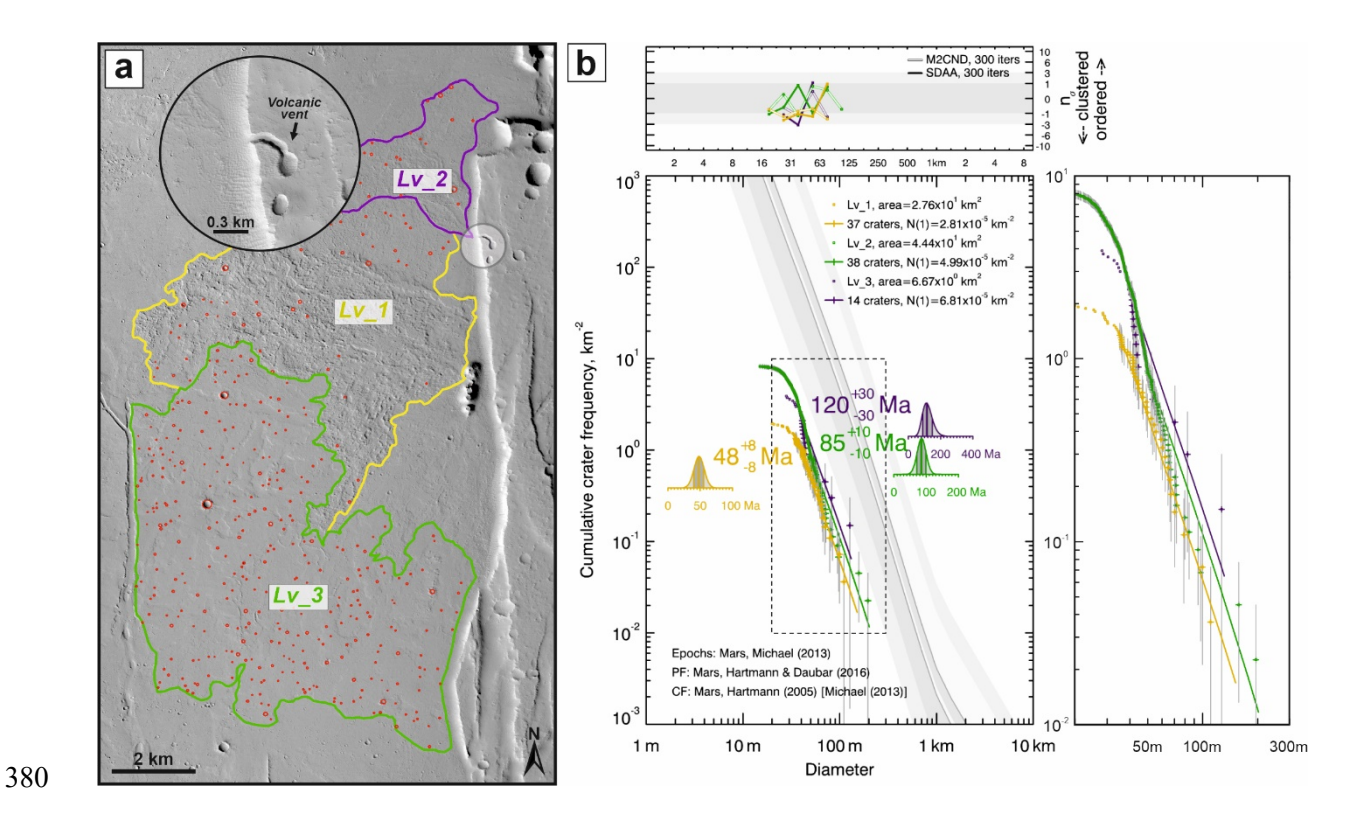


Fig. 5 (a) An overview map of the studied region illustrating the location of the lava flow units dated. The spatiotemporal relationships of these units (Lv_1, Lv_2 and Lv_3) provide age constraints on the formation of the volcanic cones. The solid lines mark the boundaries of the mapped units and their color corresponds with isochrons presented in crater-size distribution plots. The top left thumbnail is a zoom-in image showing the plausible volcanic vent and source of Lv_2. The basemap is produced using a CTX image F10_039645_2056, centered at 25.63°N and 250.28°E. **(b)** Corresponding Crater Size-Frequency Distribution plots (CSFD) with the absolute model ages determined for the three volcanic units. In all cases, the Poisson fitting technique developed by (Michael et al., 2016) was used to derive an age using the Hartmann (2005) production and chronology functions, respectively. The ± error is the 1σ age uncertainty based on the number of craters fitted. The upper panel of the CSFD plot shows the results of randomness analyses using the (inversed) standard deviation of the adjacent area (SDAA) parameter (Michael et al., 2012). The right panel is an inset of all CSFDs.

4.2. Characterization of the volcanic bombs

Our results show that the bombs are grouped into two clusters emplaced on the eastern and western flanks of the cone, CF2. They are more abundant on the eastern flank (104 identified) compared to the western flank (33 identified) and have average diameters of 2.07 ± 0.54 m (1 standard deviation; 1SD) vs. 2.90 ± 0.75 m (1SD), respectively (Table S1). In addition to the mapped bombs, we identified smaller objects likely also to be ballistically emplaced, however, their size is too small to allow for accurate measurement (see Methods). Based on the measured distances between the central point of the summit crater and the bombs, we reported that both clusters are characterized by similar dispersal distances with an average distance of 198±36 m (1SD) for the eastern flanks and 193±45 m (1SD) for the western

flanks. The minimum and maximum distances to which the bombs have been ejected are almost the same (119 m vs. 113 m and 266 m vs. 278 m for the eastern and western flanks, respectively).

4.3. Ballistic modelling

4.3.1. Use of a variable drag coefficient

To improve our understanding of the ballistic trajectories during Martian eruptions using our volcanic bombs measurements, we introduced a variable drag coefficient approach to numerical modelling calculations, in contrast to the previous assumption of a constant drag coefficient (Brož et al., 2014). To achieve this, we first adapted the ballistic model of Ogbuagu et al. (2025), originally designed for terrestrial eruptions, to account for Martian gravity and atmospheric conditions (see Section 3.4). Using the same input data, we then compared the results to the previous study on ballistically emplaced Martian pyroclasts (Brož et al., 2014) to cross-check and benchmark the results. Our calculations perfectly agree with those of Brož et al. (2014) when also using the same constant drag coefficient (C_d) assumption (Fig. 6a), validating that our model can reliably be used to investigate volcanic ballistics on Mars. Furthermore, when using a variable C_d (i.e., a more accurate description of how the particle drag changes as a function of its velocity), our model results appreciably deviate from the constant C_d results. For the different launch angles, $50^{\circ} - 80^{\circ}$, the modelled pyroclasts always reach a further distance from the source, and this deviation increases with decreased launch angles. When using a variable C_d , a 4 cm pyroclast modelled reaches 143 m, 130 m, 95 m, and 49 m further for launch angles of 50° , 60° , 70° , and 80° respectively (Fig 6b).

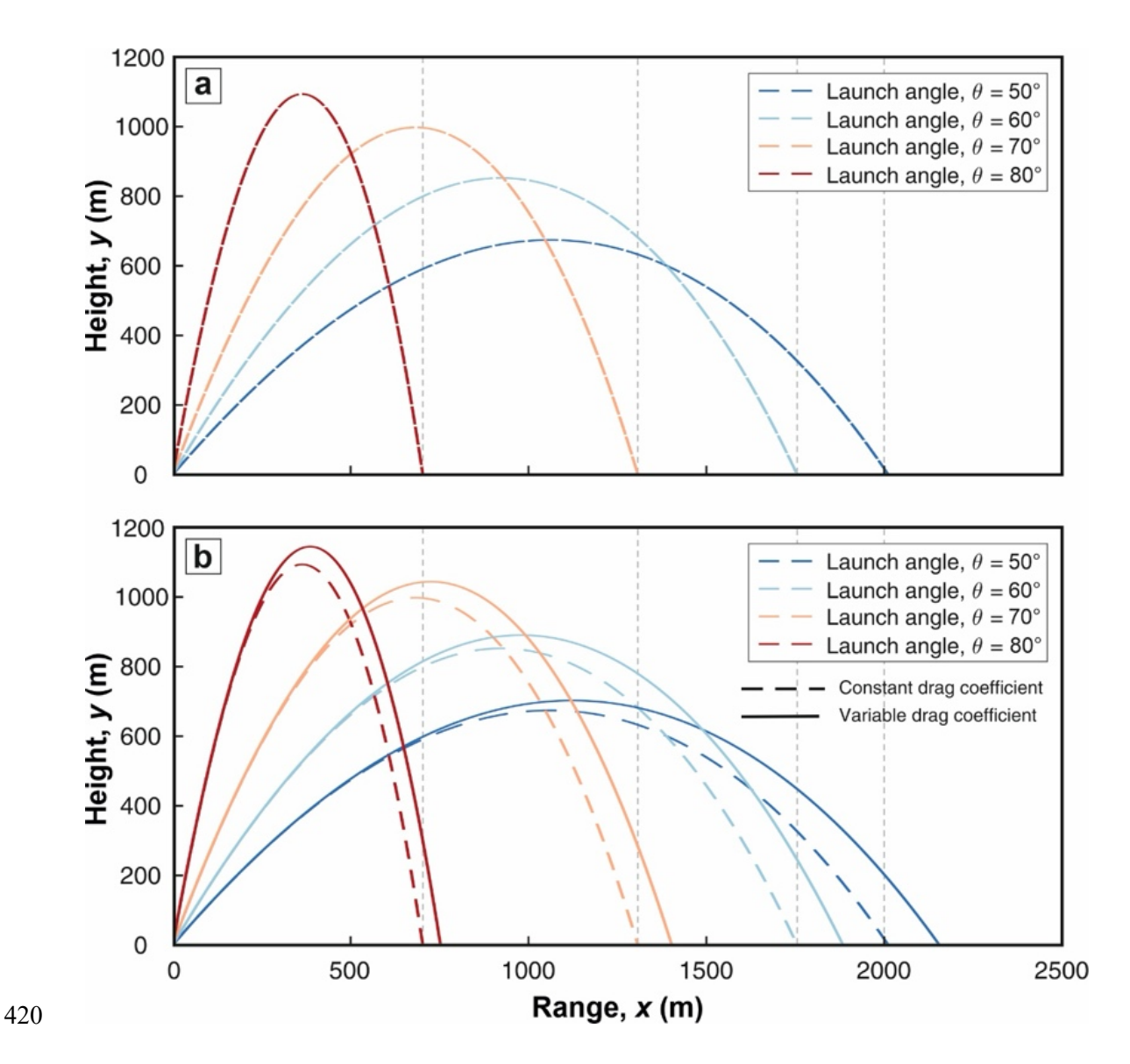


Fig. 6 (a) Ballistic pathways calculated using the model of Ogbuagu et al. (2025), including the same input parameters as Brož et al. (2014). Complete agreement between Ogbuagu et al. and Brož et al. is shown. Both panels are scaled the same, and the grey, vertical, dashed lines mark the same distance for ballistic trajectories obtained in this and Brož et al. (2014) studies. (b) Modelled trajectories of volcanic bombs on Mars using variable drag coefficients (straight lines), based on the particle Reynolds number compared with the constant drag coefficient of 0.7 (dashed lines). Model inputs are the same for both cases: d = 4 cm, bomb density, $\rho = 850$ kg m⁻³, exit velocity of 100 m s⁻¹, air density and viscosity were 0.01 kg m⁻³ and 1.3×10^{-5} Pa s, respectively.

4.3.2. Reconstructing ballistic ejection velocities

Our ballistic trajectory model was able to calculate the exit velocity and maximum height attained during flight for the 137 identified volcanic bombs. These model results were able to reproduce the observed bomb range to within \pm 1 m difference for the horizontal range, and the final bomb elevations (i.e., resting place upon landing) to within <4 m for a 37° launch angle, <7 m (for 81.8°) and <17 m (for 89°), across both densities. Given that the elevation of each bomb was established by applying the interpolation method based on the CTX-based DEM, which has an inherent uncertainty (see Methods), compared to the bomb size (>1.5 m), our model results fit well within error.

For the launch angles of 37.0° and 81.8°, the range in corresponding bomb exit velocities display a tight unimodal distribution with a mean velocity of 23 m s⁻¹ and 49 m s⁻¹, respectively. For bombs launched at angles closer to vertical i.e., the 89° launch angle, their exit velocities showed a broader distribution with a slight negative skew (Fig. 7). The mean exit velocity was 144 m s⁻¹ with about 36% of the distribution showing 160 m s⁻¹ (Fig. 7). Changes in the bomb density showed no observable differences in the distributions of the exit velocities, for a given launch angle (orange vs blue histograms in Figure 7). However, very minor deviations in the modelled exit velocities values were found across the densities 1500 and 2700 kg m⁻³. These increased from ±0.0035 m s⁻¹ for velocities within the 37° launch angle to ±0.0210 m s⁻¹ within the 81.8° angle, and ±0.232521 m s⁻¹ for the 89° launch angle.

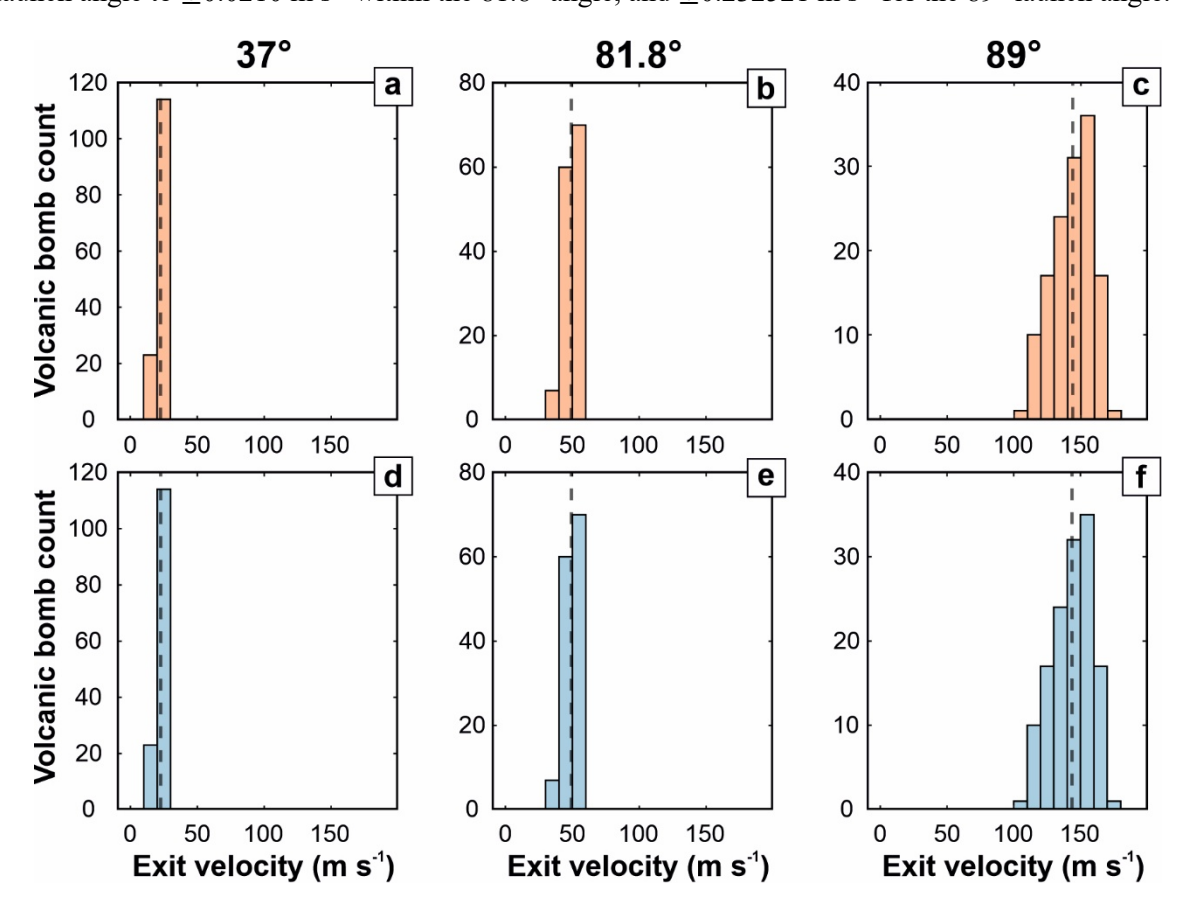


Fig. 7 Histograms of the modelled volcanic bomb exit velocities at launch angles of **(a)** 37°, **(b)** 81.8°, and **(c)** 89° for a 1500 kg m⁻³ bomb density, and **(d)** 37°, **(e)** 81.8°, and **(f)** 89° for a 2700 kg m⁻³ bomb density. Bin spacing for each subplot is 10 m s⁻¹, and each plot contains 137 velocity values. The dashed vertical lines represent the mean exit velocity for that launch angle.

The maximum height attained, again considering the three different launch angles and the two bomb densities, mostly showed a normal distribution (Fig. 8). The largest maximum height calculated for the 37° launch angle, for both bomb densities, was 37 m with a mean value of 25.2 m. With increasing the launch angle to 81.8°, the distribution of the maximum heights slightly broadened. For the 81.8° launch angle, maximum heights of 300 m to 450 m were reached by 64% of the volcanic bombs ejected. The mean maximum heights were 324.3 m for both densities at this 81.8° launch angle. The bombs launched at near-vertical angles, i.e., 89° and using varying mean densities, attained a much broader range of

maximum heights, before landing. The mean maximum heights were 2803.9 m and 2800.5 m for volcanic bombs with density 1500 kg m⁻³ and 2700 kg m³, respectively (Figs. 8c and 8f).

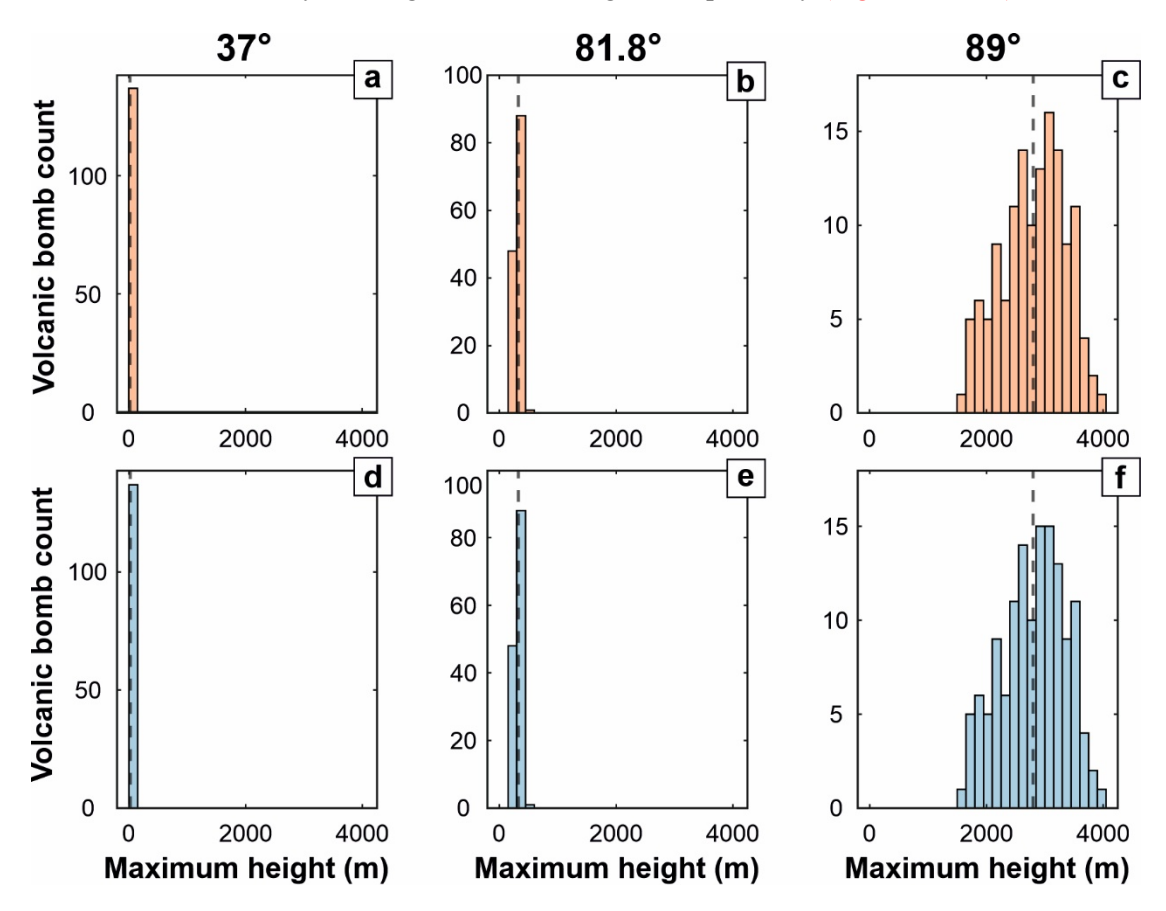


Fig. 8 Histograms of the maximum heights attained during the ballistic trajectory of volcanic bombs launched at **(a)** 37°, **(b)** 81.8°, and **(c)** 89° with bomb density of 1500 kg m⁻³, and at **(d)** 37°, **(e)** 81.8°, and **(f)** 89° with bomb density of 2700 kg m⁻³. Bin spacing for each subplot is 150 m, and each plot contains 137 values. The dashed vertical line represents the mean maximum height for that launch angle.

5. Discussion

5.1. Origin of the bombs

Although fragmented rocks near volcanic cones could be formed by collapse or erosion of the summit regions of the cones, here we contend they are volcanic pyroclasts, which here we have termed bombs. From our remotely sensed imagery, the bomb size range observed agrees with the distance decay rule, where larger pyroclasts are emplaced closer to the eruption centre, while smaller ones are found at greater distances (Fig. 2a). In the gravity-driven processes such as rolling and bouncing (Day et al., 2022), larger pyroclasts are rarely preserved on the steep upper slopes, as they are typically transported downslope and beyond the cone outlines accumulating at the base of the edifices. This is not the distribution pattern observed in this study, they form two clusters on opposite sides of the analyzed CF2 cone, suggesting ejection at similar velocities and angles (Fig. 3a-b). Furthermore, given that the slopes of our studied cones are generally below the typical angle of repose ~30° (Brož et al., 2014) and are composed of coarse, agglutinated spatter (Fig. 3d), we infer that material avalanching was relatively limited during cone construction. However, steeper slopes could have been formed locally, particularly

near the summit crater rim, potentially leading to minor slumping into a central crater (Fig. 3e). Altogether, our observations support the interpretation that the locations of these pyroclasts, which were ballistically emplaced during explosive eruptions or lava fountaining phases, record the closets possible positions of their landing.

Pyroclastic flows are also an unlikely source of the observed features, as such flows typically produce sorted, elongated deposits that follow topographic lows, rather than isolated clasts scattered across the surrounding terrain. Furthermore, the most distal, isolated pyroclasts mapped on the WNW and ENE slopes are located in areas where gravity-driven transport, either by flow or rolling, is improbable, based on the local terrain slope.

On Earth, bombs are typically interpreted as molten or semi-molten ejecta that typically deform during flight and upon impact. Whereas volcanic blocks typically refer to solid rock fragments that had already solidified before the eruption and often remain intact upon impact. For our observations on the Martian surface, it is not possible to distinguish blocks from bombs. So here we have used bombs as the all-encompassing term for volcanic pyroclasts > 64 cm in diameter.

5.2. Origin of the cones

The Martian surface hosts a variety of small-scale edifices resembling mounds or knobs, whose origin can be debated (Brož et al., 2017a; Dapremont and Wray, 2021). In most cases, their formation might have been attributed to either volcanic (Brož et al., 2021, 2017b; Brož and Hauber, 2012; Pieterek et al., 2022b) or sedimentary processes (Brož et al., 2023; Cuřín et al., 2023; Komatsu et al., 2016; Okubo, 2016). In the geological context of our studied region, Cerberus Fossae is associated with Hesperian-aged terrains fractured by the subsurface diking (Shahrzad et al., 2024) and adjacent widespread late Amazonian (<300 Ma) effusive volcanism (Hauber et al., 2011; Pieterek et al., 2022a). Given that the edifices studied here, along with the associated lava flow unit, are structurally the highest, their formation must be controlled by the subsurface extrusive processes. Since these cones resemble other small-scale volcanic cones on Mars (Brož et al., 2017b; Brož and Hauber, 2012a; Flynn and Rader, 2024), the most reasonable explanation for their origin is igneous volcanism, consistent with the geological context of the region.

The spatial alignment of the cones in the N-S direction, parallel to the Ceraunius Fossae fractures (Shahrzad et al., 2024), and the predominant elongation of the adjacent volcanic vents (Pieterek et al., 2022a; Richardson et al., 2021), indicate that the subsurface dike might have propagated according to the regional extensional component. These structural observations imply that the preexisting crustal fractures controlled the magmatism associated with the volcanic cones studied here. Similar inferences have also been made for other Martian volcanic fields (Brož and Hauber, 2012; Pieterek et al., 2022b) as well as their terrestrial counterparts (Carracedo, 1992; Opheim and Gudmundsson, 1989; Tibaldi et al., 2017). The association between the western spreading flow-like unit (Lv_1) and the cones resembles

terrestrial examples of pyroclastic cones of basaltic composition (Carracedo, 1992; Reynolds et al., 2016), indicating the contribution of at least one effusive phase during the eruption. The relatively short distance over which the mapped lava flow migrated from the cones, along with its rough and hummocky surface, distinct from the adjacent lava flows, indicates a more differentiated composition, relatively high crystallinity, or a low-effusion rate of the erupted magma. For example, based on the comparative surface analyses, a more evolved, and thus more viscous, magma has also been inferred for the central cone formed atop of the fissure eruption south of Pavonis Mons (Pieterek and Jones, 2023), as well as for pyroclastic cones associated with lava flows in Ulysses Colles (Brož and Hauber, 2012) and Coprates Chasma (Brož et al., 2017b). Altogether, this indicates that the studied cone-associated lava flow is distinct from the adjacent volcanic terrains.

The documented cones are characterized by relatively steep flanks that reach up to ~30° (Fig. 4c and S2), which is close to, and within measurement error, of the angle of repose (Brož et al., 2014). The steepest slopes (Fig. 4c) are located near the summits of the cones, exceeding the average slope values typically measured for Martian scoria cones (Brož et al., 2015). This suggests that the erupted pyroclastic material was cohesive or welded, consistent with spatter agglutination (Flynn and Rader, 2024). The two most prominent cones (CF1 & 2), yield average slope values of 14.8° and 17.1°, respectively, along their W-E axes (Fig. S2). These values are comparable to those reported by Flynn and Rader (2024) for Martian spatter cone (20.7°).

In comparative plots (Figs. 9 and 10), our cones (CF1 & 2) exhibit morphometric characteristics that are substantially distinct from other explosive-origin features documented elsewhere on Mars. In Figure 9, the cones plot within the field defined for terrestrial spatter cones (Wood, 1979), suggesting they are most likely composed of a different pyroclastic material compared to Martian scoria cones. This notion is consistent with our satellite observations (e.g., knobby texture of the summit slopes). Additionally, the morphological parameters used to differentiate volcanic edifices on Mars further support this interpretation (Fig. 10). In each case, the studied cones yield distinct parameter values relative to Martian scoria cones.

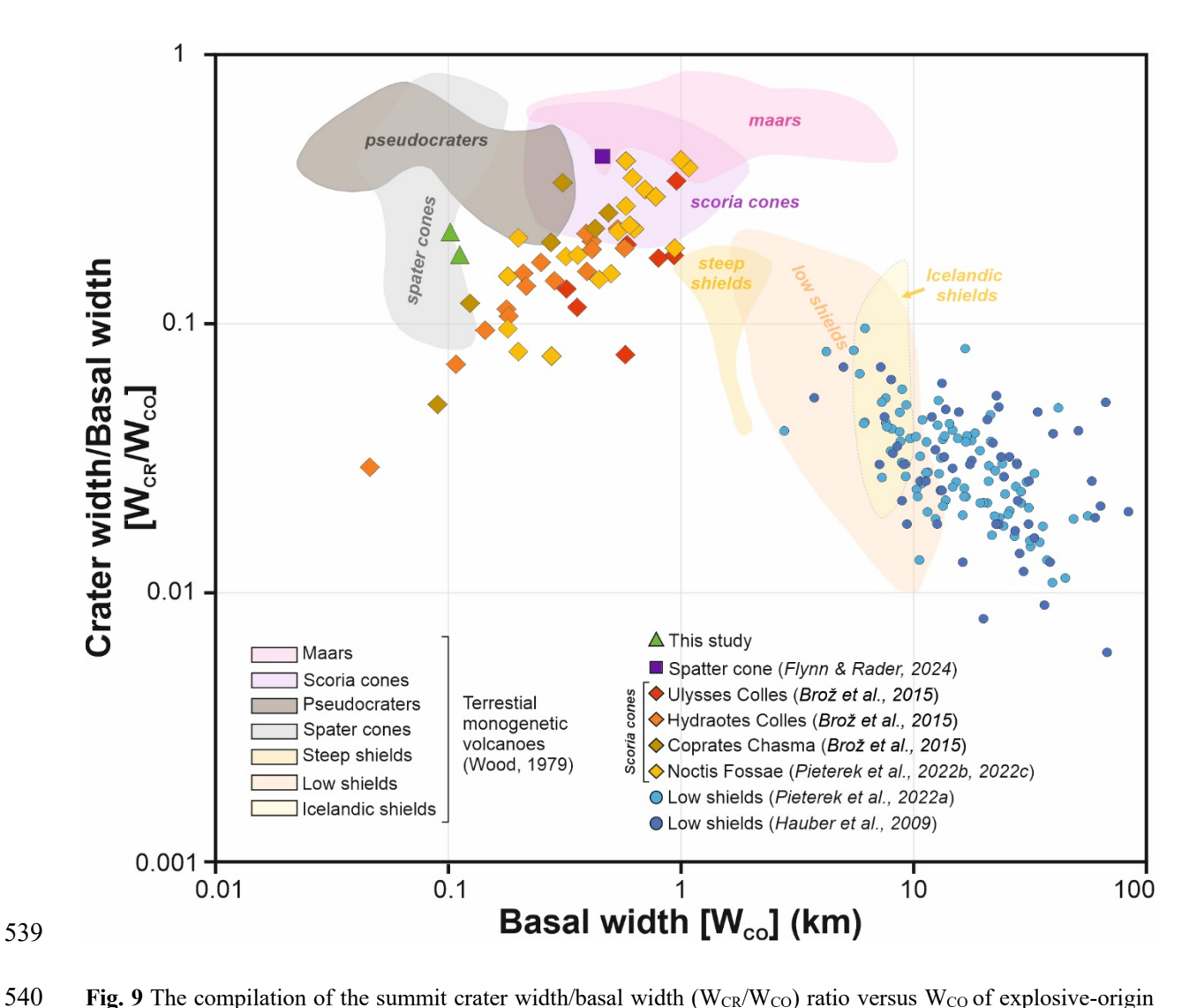


Fig. 9 The compilation of the summit crater width/basal width (W_{CR}/W_{CO}) ratio versus W_{CO} of explosive-origin edifices. The results are plotted along with various types of terrestrial monogenetic volcanoes (Wood, 1979). Data for Martian explosive-origin edifices (Brož et al., 2015; Pieterek et al., 2022b, 2022c), low shield volcanoes (Hauber et al., 2009; Pieterek et al., 2022a) and one inferred spatter cone (Flynn and Rader, 2024) has been collected from literature. Our discovered cones are shown by the green triangles. There is clear morphological evidence that the cones is Ceraunius Fossae are distinct from other scoria cones reported on Mars, potentially indicating that studied cones are composed of different pyroclastic material.

In addition to these morphometric parameters, HiRISE-based observations provide further evidence supporting the explosive origin of the cones. Close-up observations of the summit crater rim and proximal to-rim slopes reveal that the cones have a rough and knobby texture (Fig. 3d), likely resulting from the agglutination of the pyroclastic material ejected during low- to mid-explosive eruption and lava fountaining. The partially molten pyroclasts were able to agglutinate and form short, creep-like structures (Fig. 3d) that resemble rheomorphic flows (Valentine et al., 2017). This suggests that during the final stages of eruption, the summit parts of the cones might have been covered by nonwelded lapilli and bombs, which are prone to slope creep. Such creeping could have contributed to larger mass-wasting slope processes involving find-grained material, as observed on the CF3 cone (Fig. 3e).

Moreover, on the northern internal wall slopes of the CF1 & CF2 cones, we observed large fragments of rocks that could represent either fallen blocks or pyroclasts agglutinated to the inner cone walls. This suggests the cones might have been formed from relatively coarse, conglomerated materials rather than fine-grained scoria. Similar observations were made by Flynn and Rader (2024) for a volcanic cone south of Pavonis Mons, who attributed cone formation there to the agglutination of spatter. Additionally, the studied cones are accompanied by volcanic bombs, which are found both on flanks and at the base of the edifices (Figs. 2 and 3b). While no similar observations have been provided for other volcanic fields hosting the interpreted Martian scoria cones (Brož et al., 2015), such phenomena can be directly traced for the terrestrial pyroclastic cones (Galindo et al., 2013; Gurioli et al., 2013; Taddeucci et al., 2017; Vanderkluysen et al., 2012). The presence of volcanic bombs in relation to volcanic cones indicates the contribution of an energetic explosive phase during the eruption.

Moreover, we observed that some parts of the cones' flanks have V-shape structures resembling gullies (Fig. 3b-c). On Mars, these structures are thought to be associated with steep slopes (i.e., impact craters, scarps) and are formed by downslope moving fluids. Although the planet's current climate is not conducive to the melting of water ice, new findings suggest that favorable conditions might have occurred repeatedly over the past several million years, leading to periods of ice melting and CO₂ frost evaporation at different parts of the year (Dickson et al., 2023). Despite this, the similar-looking slope structures on Mars can also be attributed to granular flows, which do not require liquid water for initiation (Dundas et al., 2017). The V-shape structures formed by alluvial processes (Zarazúa-Carbajal et al., 2024) can also be developed on the flanks of terrestrial counterparts, as observed for the small-volume mafic volcanoes of the Lunar Crater volcanic field in Nevada, USA (Valentine et al., 2017).

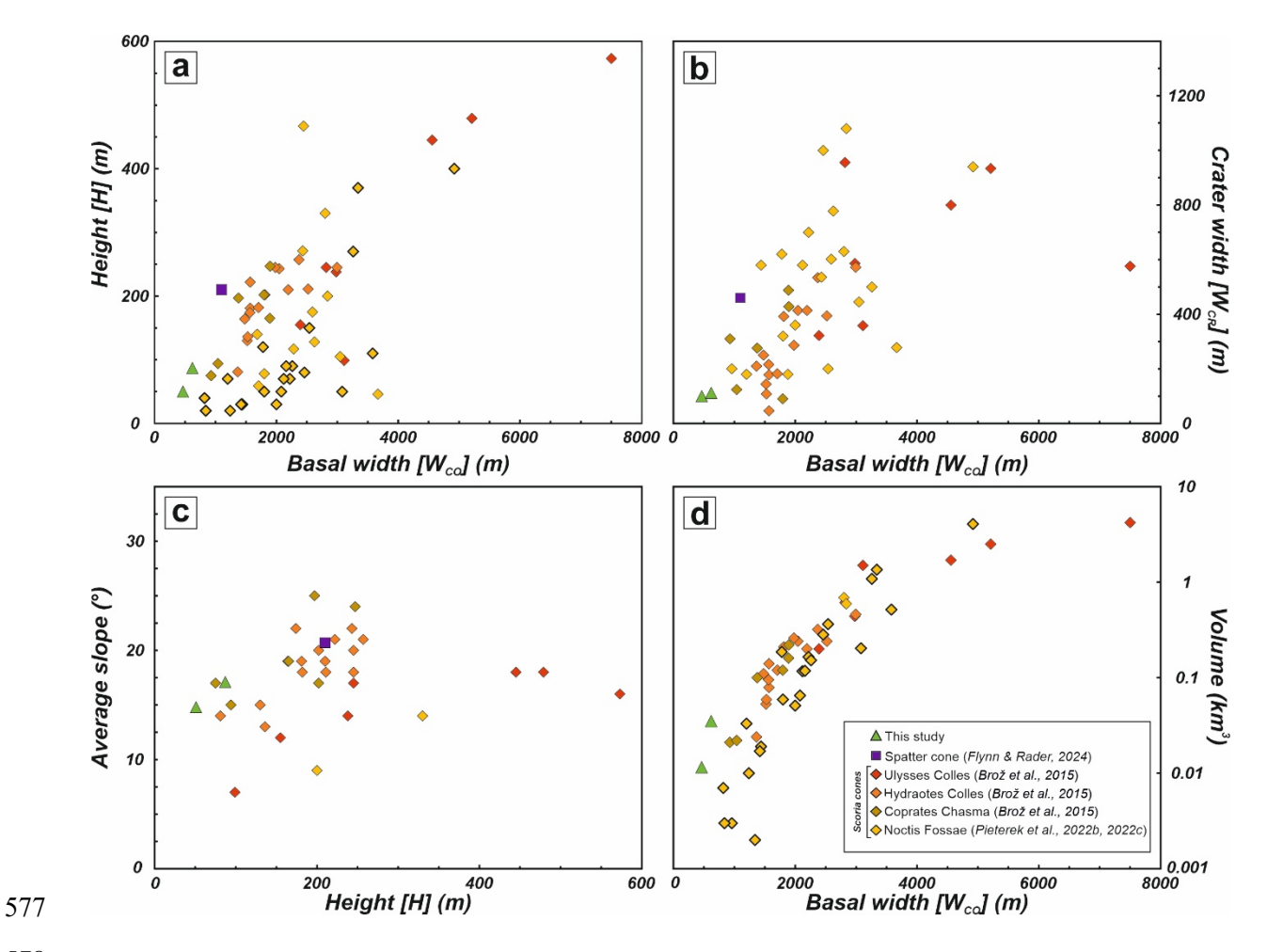


Fig. 10 Scatter plots illustrating the morphological parameters of explosive-origin edifices (scoria and spatter cones) studied across Mars with respect to the discovered cones in the Ceraunius Fossae region (green triangles). The majority of data is based on HiRISE- and CTX-based DEM measurements, whereas for the majority of Noctis Fossae cones, the height and thus the volume have been determined based on MOLA-HRSC DEM and might be characterized by lower precision due to the low resolution. The MOLA-based measurements are highlighted by thicker rims of the symbols in panels (a) and (d).

The morphological comparison with terrestrial analogs provides a powerful tool for interpreting enigmatic volcanic features observed in satellite images. To provide terrestrial counterparts to our studied features, we used Google Earth Pro, utilizing the CNES/Airbus 2021 images with a spatial resolution of ~0.5 m/pixel, which is similar to Martian satellite images of the HiRISE camera. Here, we compare our discovered edifices to the cones of the Montañas def Fuego of Timanfaya National Park, which were formed during the 1730–1736 fissure eruption in Lanzarote, Canary Islands (Carracedo, 1992). Their relatively small size is interpreted to be attributed to the high proportion of spatter-dominated material. This resulted in the scattered morphological parameters attributed to fissure-controlled eruption dynamics rather than centralized eruptions (Kervyn et al., 2012). The morphometry of these cones was modified by syn- and post-eruption processes (Carracedo, 2014; Romero et al., 2019), as reflected in the varied shapes of the cones i.e., horseshoe-shaped (Bemis and Ferencz, 2017). For instance, several-meter-sized mounds developed on the cone's flank resemble those topographic features observed on top of the CF4 cone (Fig. 11). By analogy, we interpreted this feature as a rafted

mound or cone fragment. A similar feature is also present on the southern slope of the CF1 cone and identifiable on the DEM (Fig. 3). Moreover, morphologically similar-looking cones (Fig. 11d) were formed during the Laki (Skaftár Fires) fissure eruption of 1783–1785 in southern Iceland (Thordarson and Self, 1993). The formation of these edifices is attributed to Hawaiian-style lava fountaining after mid- to low-energetic explosive eruptions, which produced alternating coarse scoria layers, each capped with a relatively thin layer of agglutinated spatter (Reynolds et al., 2016; Thordarson and Self, 1993). The spatter cones are often superimposed on earlier-formed scoria cones and tuff cones, which originated form more energetic eruptions (Thordarson and Self, 1993). Zoomed-in observations reveal that these edifices, in addition to a common shape, exhibit surface textures on their upper slopes similar to those of the Martian cones, specifically showing agglutinated spatter deposits (Fig. 11d). Altogether, this comparison shows that the considered Martian and terrestrial cones exhibit similar morphologies and summit crater rim structures (Fig. 11), suggesting that both sets of cones fields feature a combination of predominant agglutinate spatter and loose pyroclastic, scoriaceous material.

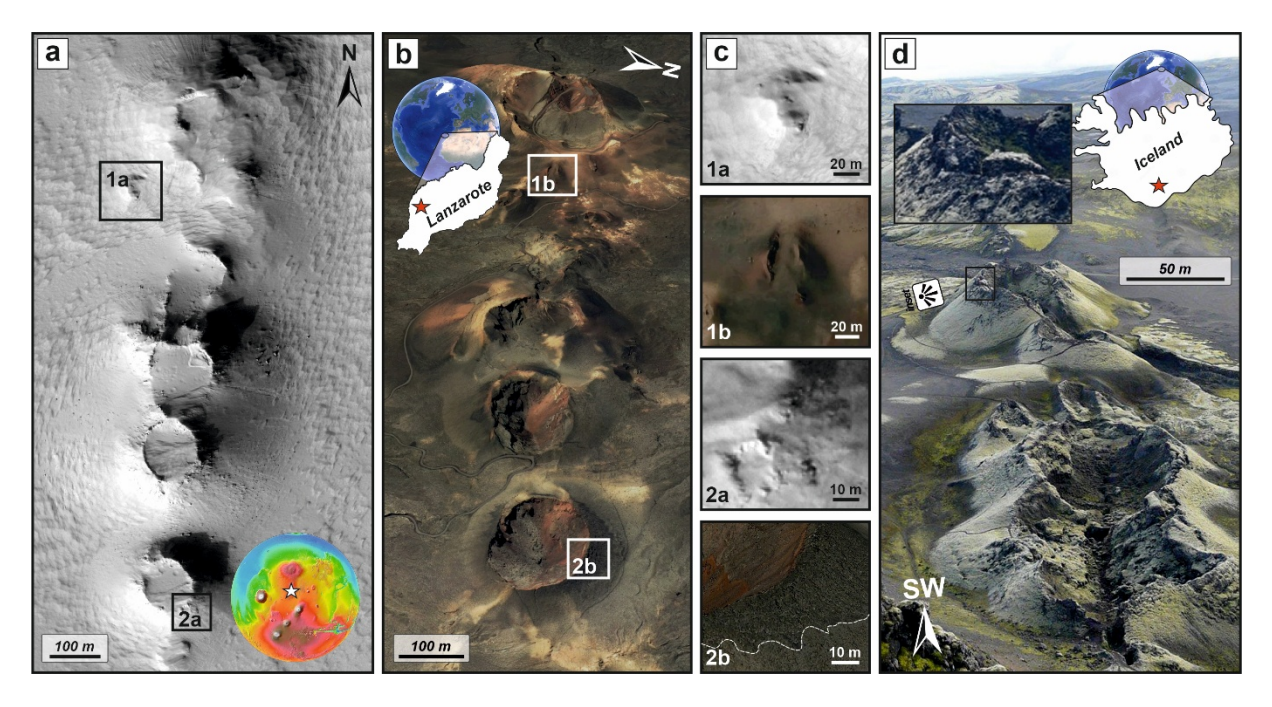


Fig. 11 (a) HiRISE image of the Cerberus Fossae cones together with the **(b)** corresponding terrestrial counterpart volcanic cones of Montaña def Fuego within the Timanfaya National Park, Lanzarote, Canary Islands. The stars placed on insets indicate the locations of regions of interest. The image of a terrestrial example has been captured in 2021 by the CNES/Airbus satellite. The rectangles mark the locations of close-up images **(c)**. The numbers refer to image pairs of comparable features. The first pair (1a & 1b) illustrates the positive topographic feature on top of the flank of the larger cone and can be interpreted as a rafted cone, whereas the second pair (2a & 2b) shows the zoom-in view of the summit crater rim with fragmented and knobby texture deposits forming the flow-like lobes. **(d)** Laki cones aligned in the NE-SW direction. The inset shows the rough and steep sided upper part of the cone's slope. Credit: pinterest.com; available on 25.07.2025.

5.3. Age constraints

The location of volcanic fields in Tharsis (i.e., Ulysses and Noctis Colles), which host conical, steepsided edifices of explosive origin are spatially associated with Hesperian-aged and fractured terrains. This suggests that elevated regions of Tharsis might have survived the widespread resurfacing by young lava flows, providing an opportunity to view older volcanism within the province (Brož and Hauber, 2011). Based on the relative stratigraphy of lava flows adjacent to Ulysses Colles, volcanic activity in the Ulysses Coles region probably occurred between 1530 and 440 Ma (Brož and Hauber, 2012). In contrast, the volcanic cones located in the Noctis Fossae region reveal a more complex temporal evolution, which is also reflected in their varied morphological preservation (Pieterek et al., 2022b). The cones formed on top of the fractured terrain of Noctis Fossae are >300 Ma, whereas the best-preserved edifices occurring north of the fractured crust are younger and likely formed between 200 and 50 Ma. Furthermore, a late Amazonian age (between 360 and 210 Ma) has also been inferred for the volcanic cones in Coprates Chasma inside Valles Marineris (Brož et al., 2017b). Together, these age results indicate that the explosive eruptions on Mars could have been restricted to specific extensional regions and occurred relatively recently. This is consistent with our findings. We reported a previously undiscovered row of young (<85 Ma) pyroclastic cones emplaced adjacent to the old (2.2 ± 0.2 Ga; Shahrzad et al. (2024)) Ceraunius Fossae terrains (Fig. 5). The cones described here were formed after effusive eruptions originated from nearby volcanic vents, which took place less than 100 million years ago (Hauber et al., 2011; Pieterek et al., 2022a). The specific lava flow sourced from our cones was found to be 48 Ma lava flow (Lv1) suggesting that the cones were also constructed at this time, or very shortly after. The coexistence of effusive and explosive eruptions in Tharsis has also been reported for an inferred spatter cone south of Pavonis Mons (Flynn and Rader, 2024). This edifice is most likely attributed to the activity of distributed volcanism on top of the Pavonis Mons apron, which has been dated as young as <100 Ma (Pieterek et al., 2022a). Therefore, the studied cones constitute another piece of evidence demonstrating relatively common late Amazonian explosive eruptions, consistent with the widespread identification of very recent (mostly <100 Ma, but sometimes as young as 25 Ma) spatter ramparts developed around the summit vents of low shield volcanoes (Pieterek and Jones, 2024).

5.4. Volcanic ballistic trajectory modelling and its uncertainties

624

625

626

627

628

629

630

631

632

633

634

635

636

637

638

639

640

641

642

643644

645

646

647

648

649

650

651

652

653

654

655

656

657

658

659

The discovered cones constitute a unique Martian natural laboratory to use ballistic trajectory models. Although the resolution of the HiRISE images does not allow identification of individual pyroclasts smaller than 1.5 m in diameter, we investigated the spatial distribution of the bombs >1.5 m in diameter located on the flanks and at the base of the cones (Fig. 2). While the original landing location of these bombs could have been modified by gravity-driven processes (Day et al., 2022), the satellite observations do not support this scenario. These bombs are not associated with any surficial features, such as rolling or bouncing tracks, which would suggest a mass wasting origin. However, it is important to note that such surface features have low preservation potential and could have been obscured by dust or subsequent eruptions producing fine-grained material, limiting their detectability.

Specifically, we found that the CF2 cone shows two clusters of bombs located on the eastern and western flanks. The eastern flank cluster contains 104 bombs with a 2.07 ± 0.54 m (1SD) average diameter, whereas the western flank cluster only contains 33 bombs with a larger average diameter of

 2.90 ± 0.75 m (1SD). Within each cluster, the sizes of the bombs are also varied, which is typical for terrestrial systems (Galindo et al., 2013; Gurioli et al., 2013; Taddeucci et al., 2017). The difference between the clusters could indicate that they were ejected during two independent eruption events or episodes, likely characterized by different explosion energies.

660

661662

663

664

665

666667

668

669

670671

672

673

674

675

676

677

678

679

680

681

682

683

684

685

686

687

688

689

690691

692693

694

695

Here, by using parameters obtained for the mapped volcanic bombs, such as size, distance from the vent, and elevation difference from the source, we employed a ballistic trajectory model to calculate eruption parameters for the CF2 spatter cone. Based on model ballistic pathways for pyroclast transport on Earth and Mars, it has been reported that the Martian pyroclastic material would be ejected ~37 times higher and transported ~26 times farther than on Earth (Brož et al., 2014; Flynn and Rader, 2024). This leads to the formation of larger volcanic edifices with less steep slopes compared to the terrestrial counterparts (Brož et al., 2014; Wilson and Head, 1994). Indeed, our studied cones are most likely composed of spatter, and they are larger than their terrestrial counterparts (Fig. 9). Numerical tests provided by Brož et al. (2014) showed that the involvement of the drag reduction in the modelling is especially important for less-energetic explosions that eject particles with smaller velocities over shorter distances. This is because the drag effect impacts a larger fraction of the total trajectory. As the studied cones in the Ceraunius Fossae region are among the smallest pyroclastic-origin cones on Mars and are inferred to be composed of coarser pyroclasts, we recognize that including a variable drag coefficient is crucial for obtaining more accurate eruption parameters. The model of Ogbuagu et al. (2025) used here, but adapted for Martian atmospheric conditions and gravity, includes a variable drag coefficient. This means that the drag experienced by the ejected particle is related to its velocity at all locations along its trajectory. A comparison between our model and that of Broz et al. (2014) shows that when a variable drag coefficient is applied, the transport distance for small pyroclasts (4 cm in diameter) is always greater than in the Broz et al.'s model, and this deviation increases with decreased launch angles. This finding is consistent with previous considerations and models (Brož et al., 2014; Wilson and Head, 1994), which argued that the lower gravitational acceleration and atmospheric density on Mars result in higher exit velocities of ejected pyroclasts.

As evidenced by Brož et al. (2014), the shape of volcanic cones formed by explosive activity mainly depends on the launch angle, pyroclast size, and exit velocity. Larger pyroclasts are expected to accumulate closer to the vent, suggesting that the cone size is likely proportional to the range of potential ballistic trajectories, assuming a given exit velocity. The calculations of Flynn and Rader (2024) showed that larger pyroclasts (20 cm in diameter and a density of ~1946 kg/m³) compared to those considered by Brož et al. (2014) (4 cm in diameter and density of 850 kg/cm³), both ejected at velocities of 100 m s⁻¹ and launch angle of 80°, have a shorter transport distance by ~2.3 times and lower maximum height attained during eruption by a factor of ~2. This points out that less energetic explosive eruptions (i.e., those with smaller exit velocities) or the ejection of coarser pyroclasts (>20 cm in diameter) would result in shorter ballistic trajectories, which is the case in this study. Additionally, our model results showed

that large changes in the bomb/pyroclast density (from 1500 to 2700 kg m⁻³) have no observable influence in the distributions of the exit velocities, for a specific launch angle (Fig. 7).

According to our model results the volcanic bombs (>1.5 m in diameter) we detected on the HiRISE image, were launched with mean exit velocities ranging from 23 m s⁻¹ (at 37.0°), through 49 m s⁻¹ (at 81.8°) to 144 m s⁻¹ (at 89.0°) (Fig. 7). The mean exit velocity calculated for all launch angles and pyroclast densities is 72 m s⁻¹. These results fall within the range of those proposed by Brož et al. (2014), who inferred that the most Martian plausible ejection velocities are approximately twice those on Earth. Moreover, the mean maximum heights attained during the eruption, calculated in this study (Fig. 8), are comparable with the results provided by Brož et al. (2014) and Flynn and Rader (2024), considering the larger size of the pyroclastic bombs we examined. Therefore, we argue that the detailed measurements characterizing the emplacement of volcanic bombs, with a clear spatial relationship with the pyroclastic cones, provide a means to validate and improve our understanding of ballistic trajectories and the distances over which pyroclastic material can be transported on Mars. In this study, we demonstrated how direct observations of volcanic bombs enabled us to quantitatively determine the exit velocities and maximum height attained during the eruption.

6. Conclusions

Here, we investigated the previously unstudied small-scale, conical-shaped volcanic edifices, which can be interpreted as having been formed by the accumulation of spatter. Such a pyroclastic material is coarser-grained compared to the typical pyroclastic material accounted for the Martian scoria cones, suggesting less lava fragmentation during eruption. The discovery of the young, late Amazonian-aged explosive origin cones associated with lava flow dated to 48 Ma provides evidence that this volcanic system experienced both explosive and effusive eruptions, likely occurring close together in time and possibly simultaneously.

The cones imaged by the HiRISE camera are accompanied by the pyroclasts interpreted as volcanic bombs, located on the flanks and at the base of the cones. Despite certain limitations of remote sensing observations and related interpretations, such as dust accumulation or subsequent eruptions producing fine-grained material that may obscure secondary processes like downslope rolling, the current positions of the mapped volcanic bombs likely represent their original landing sites. Therefore, we argue that these bombs were ballistically ejected during an explosive eruption. The identification of these volcanic bombs enabled us to use a ballistic trajectory model to determine their mean exit velocities and maximum height attained during flight. To provide the most accurate model results, we incorporated a variable drag coefficient, which accounts for how particle drag changes as a function of velocity—particularly important for coarse-grained pyroclasts ejected and deposited close to the vent. Hence, our results provide quantitative constraints on Martian explosive eruptivity, supported by direct observations.

These findings also offer a means to refine our understanding of ballistic trajectories and distances over which the pyroclastic material can be transported on Mars. High-resolution remotely sensed volcanological mapping could thus be essential for establishing eruption dynamics and, consequently, the magma fragmentation. Our study therefore presents an important step forward in understanding the formation of predominantly explosive edifices on Mars and highlights a need for further studies aimed at discovering pyroclasts such as volcanic bombs, which would provide datasets for verifying ballistic models and understanding the associated volatile release.

Acknowledgments

738

746

- We thank editor Nicolas Mangold for guidance during the evaluation of the manuscript, as well as Ian
- 740 Flynn and an anonymous reviewer for their thorough and insightful comments, which helped improve
- the manuscript. We acknowledge the Planetary Data System teams for sharing data. This project has
- been conducted in the frame of the preparation and first phase of the MARIVEL grant No.
- 743 2024/53/B/ST10/00488 funded by the National Science Centre of Poland. BP was supported by a
- 744 START scholarship funded by the Foundation for Polish Science (FNP). TJJ was supported by a UK
- Research and Innovation Future Leaders Fellowship (MR/W009781/1).

Data Availability Statement

- 747 Data used for geological mapping in this study are freely available at the NASA Planetary Data System
- 748 website. The CTX-based DEM used for topographic measurements and 3D visualizations has been
- 749 produced using Mars System of Information. The produced DEMs are available at the MarsSI repository
- and can be found together with Supplementary Data files in the Figshare online open-access repository
- 751 at 10.6084/m9.figshare.28737728.

752 References

- 753 Almeida, M.P., Parteli, E.J.R., Andrade, J.S., Herrmann, H.J., 2008. Giant saltation on Mars.
- Proceedings of the National Academy of Sciences 105, 6222–6226.
- 755 Bemis, K.G., Ferencz, M., 2017. Morphometric analysis of scoria cones: The potential for inferring
- 756 process from shape. Geol Soc Spec Publ 446, 61–100. https://doi.org/10.1144/SP446.9
- Biringen, S., Chow, C.Y., 2011. An Introduction to Computational Fluid Mechanics by Example. Wiley,
- 758 New Jersey. https://doi.org/10.1002/9780470549162
- 759 Bleacher, J.E., Greeley, R., Williams, D.A., Cave, S.R., Neukum, G., 2007. Trends in effusive style at
- the Tharsis Montes, Mars, and implications for the development of the Tharsis province. J Geophys
- Res Planets 112, E09005. https://doi.org/10.1029/2006JE002873
- Bombrun, M., Harris, A., Gurioli, L., Battaglia, J., Barra, V., 2015. Anatomy of a Strombolian eruption:
- Inferences from particle data recorded with thermal video. J Geophys Res Solid Earth 120, 2367–
- 764 2387. https://doi.org/10.1002/2014JB011037

- Bridges, N.T., Banks, M.E., Beyer, R.A., Chuang, F.C., Noe Dobrea, E.Z., Herkenhoff, K.E.,
- Keszthelyi, L.P., Fishbaugh, K.E., McEwen, A.S., Michaels, T.I., Thomson, B.J., Wray, J.J., 2010.
- Aeolian bedforms, yardangs, and indurated surfaces in the Tharsis Montes as seen by the HiRISE
- 768 Camera: Evidence for dust aggregates. Icarus 205, 165–182.
- 769 https://doi.org/10.1016/j.icarus.2009.05.017
- Brož, P., Bernhardt, H., Conway, S.J., Parekh, R., 2021. An overview of explosive volcanism on Mars.
- 771 Journal of Volcanology and Geothermal Research 409, 107125.
- 772 https://doi.org/10.1016/j.jvolgeores.2020.107125
- Brož, P., Čadek, O., Hauber, E., Rossi, A.P., 2015. Scoria cones on Mars: Detailed investigation of
- morphometry based on high-resolution digital elevation models. J. Geophys. Res. Planets 120,
- 775 1512–1527. https://doi.org/doi:10.1002/2015JE004873
- Brož, P., Čadek, O., Hauber, E., Rossi, A.P., 2014. Shape of scoria cones on Mars: Insights from
- 777 numerical modeling of ballistic pathways. Earth Planet Sci Lett 406, 14-23
- 778 https://doi.org/10.1016/j.epsl.2014.09.002
- Brož, P., Fawdon, P., Čadek, O., 2017a. Kilometer-sized cones on Mars: igneous or mud volcanoes?,
- in: European Planetary Science Congress 2017. pp. EPSC2017-107–1.
- 781 Brož, P., Hauber, E., 2012. A unique volcanic field in Tharsis, Mars: Pyroclastic cones as evidence for
- 782 explosive eruptions. Icarus 218, 88–99. https://doi.org/10.1016/j.icarus.2011.11.030
- 783 Brož, P., Hauber, E., 2011. Windows of old fractured crust and associated volcanism in Tharsis, Mars,
- 784 in: European Planetary Science Congress. p. EPSC-DPS2011-742-1.
- 785 https://doi.org/10.1029/2011GL047310
- Brož, P., Hauber, E., Wray, J.J., Michael, G., 2017b. Amazonian volcanism inside Valles Marineris on
- 787 Mars. Earth Planet Sci Lett 473, 122–130. https://doi.org/10.1016/j.epsl.2017.06.003
- 788 Brož, P., Oehler, D., Mazzini, A., Hauber, E., Komatsu, G., Etiope, G., Cuřín, V., 2023. An overview
- of sedimentary volcanism on Mars. Earth Surface Dynamics 11, 633-661.
- 790 https://doi.org/10.5194/egusphere-2022-1458
- 791 Carnahan, B., Luther, H.A., Wilkes, J.O., 1969. Applied numerical methods. Wiley New York, New
- 792 York City.
- 793 Carracedo, J.C., 2014. The 1730-1736 eruption of Lanzarote, Canary Islands, in: Gutiérrez, F.,
- Gutiérrez, M. (Eds.), Landscapes and Landforms of Spain. Springer, pp. 273–288.
- 795 Carracedo, J.C., 1992. The 1730–1736 Eruption of Lanzarote, Canary Islands. Journal od Volcanology
- 796 and Geothermal Research 53, 239–250. https://doi.org/10.1007/978-94-017-8628-7 23

- 797 Crown, D.A., Ramsey, M.S., 2017. Morphologic and thermophysical characteristics of lava flows
- southwest of Arsia Mons, Mars. Journal of Volcanology and Geothermal Research 342, 13–28.
- 799 https://doi.org/10.1016/j.jvolgeores.2016.07.008
- 800 Cuřín, V., Brož, P., Hauber, E., Markonis, Y., 2023. Mud flows in Southwestern Utopia Planitia, Mars.
- 801 Icarus 389. https://doi.org/10.1016/j.icarus.2022.115266
- Dapremont, A.M., Wray, J.J., 2021. Igneous or Mud Volcanism on Mars? The Case Study of Hephaestus
- 803 Fossae. J Geophys Res Planets 126, e2020JE006390. https://doi.org/10.1029/2020JE006390
- Day, J.M.D., Geiger, H., Troll, V.R., Perez-Torrado, F.J., Aulinas, M., Gisbert, G., Carracedo, J.C.,
- 805 2022. Bouncing spallation bombs during the 2021 La Palma eruption, Canary Islands, Spain. Earth
- Science, Systems and Society 2, 10063. https://doi.org/10.3389/esss.2022.10063
- Dickson, J.L., Ehlmann, B.L., Kerber, L., Fassett, C.I., 2024. The Global Context Camera (CTX) Mosaic
- of Mars: A Product of Information-Preserving Image Data Processing. Earth and Space Science
- 809 11, e2024EA003555. https://doi.org/10.1029/2024EA003555
- Dickson, J.L., Palumbo, A.M., Head, J.W., Kerber, L., Fassett, C.I., Kreslavsky, M.A., 2023. Gullies on
- Mars could have formed by melting of water ice during periods of high obliquity. Science (1979)
- 812 380, 1363–1367. https://doi.org/10.1126/science.abk2464
- Dundas, C.M., McEwen, A.S., Chojnacki, M., Milazzo, M.P., Byrne, S., McElwaine, J.N., Urso, A.,
- 814 2017. Granular flows at recurring slope lineae on Mars indicate a limited role for liquid water. Nat
- 815 Geosci 10, 903–907. https://doi.org/10.1038/s41561-017-0012-5
- 816 Edgett, K.S., 2009. Mars Reconnaissance Orbiter (MRO) Context Camera (CTX) observations
- regarding volcanic landforms on Mars, in: Geological Society of America Abstracts. p. 708.
- 818 Edgett, K.S., Christensen, P.R., 1991. The particle size of Martian aeolian dunes. J Geophys Res Planets
- 819 96, 22765–22776.
- 820 Fergason, R.L., Hare, T.M., Laura, J., 2018. HRSC and MOLA Blended Digital Elevation Model at
- 821 200m v2. [WWW Document]. Astrogeology PDS Annex, U.S. Geological Survey. URL
- http://bit.ly/HRSC MOLA Blend v0
- 823 Flynn, I.T.W., Crown, D.A., Ramsey, M.S., 2022. Determining Emplacement Conditions and Vent
- Locations for Channelized Lava Flows Southwest of Arsia Mons. J Geophys Res Planets 127,
- 825 e2022JE007467. https://doi.org/10.1029/2022JE007467
- Flynn, I.T.W., Rader, E., 2024. Evidence of a Martian spatter cone south of Pavonis Mons. Icarus 424,
- 827 116286. https://doi.org/10.1016/j.icarus.2024.116286
- 828 Galindo, I., Romero, M.C., Sánchez, N., Dóniz, J., Yepes, J., Morales, J.M., Becerril, L., 2013.
- Morphology and distribution of volcanic bombs in Caldera Quemada de Arriba (Lanzarote, Canary

- Islands): implications for volcanic hazard analysis, in: Santamarta-Cerezal, J.C., Gutiérrez, L.E.H.
- 831 (Eds.), Environmental Security, Geological Hazards and Management.
- 832 Golder, K.B., Burr, D.M., Kattenhorn, S.A., 2020. Investigation of target property effects on crater
- populations in long lava flows: A study in the Cerberus region, Mars, with implications for magma
- 834 source identification. Icarus 335, 113388. https://doi.org/10.1016/j.icarus.2019.113388
- 635 Goldstein, S., 1938. Modern developments in fluid dynamics: an account of theory and experiment
- relating to boundary layers, turbulent motion and wakes. Clarendon Press, Oxford.
- 837 Gurioli, L., Harris, A.J.L., Colò, L., Bernard, J., Favalli, M., Ripepe, M., Andronico, D., 2013.
- Classification, landing distribution, and associated flight parameters for a bomb field emplaced
- during a single major explosion at Stromboli, Italy. Geology 41, 559–562.
- https://doi.org/10.1130/G33967.1
- Hartmann, W.K., 2005. Martian cratering 8: Isochron refinement and the chronology of Mars. Icarus
- 842 174, 294–320. https://doi.org/10.1016/j.icarus.2004.11.023
- Hauber, E., Bleacher, J., Gwinner, K., Williams, D., Greeley, R., 2009. The topography and morphology
- of low shields and associated landforms of plains volcanism in the Tharsis region of Mars. Journal
- 845 of Volcanology and Geothermal Research 185, 69–95.
- 846 https://doi.org/10.1016/j.jvolgeores.2009.04.015
- Hauber, E., Brož, P., Jagert, F., Jodowski, P., Platz, T., 2011. Very recent and wide-spread basaltic
- 848 volcanism on Mars. Geophys Res Lett 38, 1–5. https://doi.org/10.1029/2011GL047310
- 849 Kervyn, M., Ernst, G.G.J., Carracedo, J.C., Jacobs, P., 2012. Geomorphometric variability of
- "monogenetic" volcanic cones: Evidence from Mauna Kea, Lanzarote and experimental cones.
- 851 Geomorphology 136, 59–75. https://doi.org/10.1016/j.geomorph.2011.04.009
- Kneissl, T., Van Gasselt, S., Neukum, G., 2011. Map-projection-independent crater size-frequency
- determination in GIS environments New software tool for ArcGIS. Planet Space Sci 59, 1243–
- 854 1254. https://doi.org/10.1016/j.pss.2010.03.015
- Komatsu, G., Okubo, C.H., Wray, J.J., Ojha, L., Cardinale, M., Murana, A., Orosei, R., Chan, M.A.,
- 856 Ormö, J., Gallagher, R., 2016. Small edifice features in Chryse Planitia, Mars: Assessment of a
- mud volcano hypothesis. Icarus 268, 56–75. https://doi.org/10.1016/j.icarus.2015.12.032
- Krishnan, V., Kumar, P.S., 2022. Long-Lived and Continual Volcanic Eruptions, Tectonic Activity, Pit
- 859 Chains Formation, and Boulder Avalanches in Northern Tharsis Region: Implications for Late
- Amazonian Geodynamics and Seismo-Tectonic Processes on Mars. J Geophys Res Planets 128,
- 861 e2022JE007511. https://doi.org/10.1029/2022JE007511

- Malin, M.C., Bell, J.F., Cantor, B.A., Caplinger, M.A., Calvin, W.M., Clancy, R.T., Edgett, K.S.,
- Edwards, L., Haberle, R.M., James, P.B., Lee, S.W., Ravine, M.A., Thomas, P.C., Wolff, M.J.,
- 2007. Context Camera Investigation on board the Mars Reconnaissance Orbiter. J Geophys Res
- Planets 112, E05S04. https://doi.org/10.1029/2006JE002808
- Mangold, N., Loizeau, D., Poulet, F., Ansan, V., Baratoux, D., LeMouelic, S., Bardintzeff, J.M.,
- Platevoet, B., Toplis, M., Pinet, P., Masson, P., Bibring, J.P., Gondet, B., Langevin, Y., Neukum,
- 6., 2010. Mineralogy of recent volcanic plains in the Tharsis region, Mars, and implications for
- 869 platy-ridged flow composition. Earth Planet Sci Lett 294, 440–450.
- https://doi.org/10.1016/j.epsl.2009.07.036
- McEwen, A.S., Eliason, E.M., Bergstrom, J.W., Bridges, N.T., Hansen, C.J., Delamere, W.A., Grant,
- J.A., Gulick, V.C., Herkenhoff, K.E., Keszthelyi, L., Kirk, R.L., Mellon, M.T., Squyres, S.W.,
- Thomas, N., Weitz, C.M., 2007. Mars Reconnaissance Orbiter's High Resolution Imaging Science
- 874 Experiment (HiRISE). J Geophys Res 112, E05S02. https://doi.org/10.1029/2005JE002605
- Michael, G.G., Kneissl, T., Neesemann, A., 2016. Planetary surface dating from crater size-frequency
- 876 distribution measurements: Poisson timing analysis 277, 279–285.
- https://doi.org/10.1016/j.icarus.2016.05.019
- Michael, G.G., Neukum, G., 2010. Planetary surface dating from crater size frequency distribution
- measurements: Partial resurfacing events and statistical age uncertainty. Earth Planet Sci Lett 294,
- 880 223–229. https://doi.org/10.1016/j.epsl.2009.12.041
- Michael, G.G., Platz, T., Kneissl, T., Schmedemann, N., 2012. Planetary surface dating from crater size-
- frequency distribution measurements: Spatial randomness and clustering. Icarus 218, 169–177.
- https://doi.org/10.1016/j.icarus.2011.11.033
- Mouginis-Mark, P.J., Zimbelman, J.R., Crown, D.A., Wilson, L., Gregg, T.K.P., 2022. Martian
- 885 volcanism: Current state of knowledge and known unknowns. Geochemistry 82, 125886.
- https://doi.org/10.1016/j.chemer.2022.125886
- 887 Ogbuagu, C.C., Lin, K.C., Jones, T.J., De Angelis, S., 2025. In-flight pyroclast cooling during mafic
- 888 explosive eruptions: a numerical model. Journal of Volcanology and Geothermal Research
- 889 VOLGEO-D-25-00074.
- 890 Okubo, C.H., 2016. Morphologic evidence of subsurface sediment mobilization and mud volcanism in
- 891 Candor and Coprates Chasmata, Valles Marineris, Mars. Icarus 269, 23–37.
- 892 https://doi.org/10.1016/j.icarus.2015.12.051
- 893 Opheim, J.A., Gudmundsson, A., 1989. Formation and geometry of fractures, and related volcanism, of
- the Krafla fissure swarm, northeast Iceland. Geol Soc Am Bull 101, 1608–1622.
- 895 https://doi.org/10.1130/0016-7606(1989)101<1608:FAGOFA>2.3.CO;2

- Pantaleone, J., Messer, J., 2011. The added mass of a spherical projectile. Am J Phys 79, 1202–1210.
- Peters, S.I., Christensen, P.R., Clarke, A.B., 2021. Lava Flow Eruption Conditions in the Tharsis
- 898 Volcanic Province on Mars. J Geophys Res Planets 126, e2020JE006791.
- 899 https://doi.org/10.1029/2020JE006791
- Petrosyan, A., Galperin, B., Larsen, S.E., Lewis, S.R., Määttänen, A., Read, P.L., Renno, N., Rogberg,
- 901 L.P.H.T., Savijärvi, H., Siili, T., Spiga, A., Toigo, A., Vázquez, L., 2011. The Martian atmospheric
- 902 boundary layer. Rev. Geophys 49, 3005. https://doi.org/10.1029/2010RG000351
- Pieterek, B., Brož, P., Hauber, E., Stephan, K., 2024a. Insight from the Noachian-aged fractured crust
- to the volcanic evolution of Mars: A case study from the Thaumasia graben and Claritas Fossae.
- 905 Icarus 407, 115770. https://doi.org/10.1016/j.icarus.2023.115770
- Pieterek, B., Ciazela, J., Lagain, A., Ciazela, M., 2022a. Late Amazonian dike-fed distributed volcanism
- 907 in the Tharsis volcanic province on Mars. Icarus 386, 115151.
- 908 https://doi.org/10.1016/j.icarus.2022.115151
- 909 Pieterek, B., Jones, T.J., 2024. Mildly explosive eruptions at Martian low-shield volcanoes Check for
- 910 updates. Commun Earth Environ 5, 542. https://doi.org/10.1038/s43247-024-01697-w
- Pieterek, B., Jones, T.J., 2023. The evolution of Martian fissure eruptions and their plumbing systems.
- 912 Earth Planet Sci Lett 621, 118382. https://doi.org/10.1016/j.epsl.2023.118382
- Pieterek, B., Jones, T.J., Wilson, L., 2024b. The Morphology of Martian Volcanic Ramparts and Their
- 914 Use in Determining Vent-Proximal Eruption Dynamics. J Geophys Res Planets 129,
- 915 e2023JE008233. https://doi.org/10.1029/2023JE008233
- Pieterek, B., Laban, M., Ciążela, J., Muszyński, A., 2022b. Explosive volcanism in Noctis Fossae on
- 917 Mars. Icarus 375, 114851. https://doi.org/doi.org/10.1016/j.icarus.2021.114851
- Pieterek, B., Laban, M., Ciążela, J., Muszyński, A., 2022c. Widespread explosive volcanism in Noctis
- Fossae on Mars, in: 53rd Annual Lunar and Planetray Science Conference. p. 1375.
- 920 https://doi.org/10.7868/s0453881113020068
- 921 Quantin-Nataf, C., Lozac, L., Thollot, P., Loizeau, D., Bultel, B., Fernando, J., Allemand, P., Dubuffet,
- 922 F., Poulet, F., Ody, A., Clenet, H., Leyrat, C., Harrisson, S., 2018. MarsSI: Martian surface data
- processing information system. Planet Space Sci 150, 157–170.
- 924 https://doi.org/10.1016/j.pss.2017.09.014
- Reynolds, P., Brown, R.J., Thordarson, T., Llewellin, E.W., 2016. The architecture and shallow conduits
- of Laki-type pyroclastic cones: insights into a basaltic fissure eruption. Bull Volcanol 78, 36.
- 927 https://doi.org/10.1007/s00445-016-1029-0

- 928 Richardson, J.A., Bleacher, J.E., Connor, C.B., Glaze, L.S., 2021. Small Volcanic Vents of the Tharsis
- 929 Volcanic Province, Mars. J Geophys Res Planets 126, e2020JE006620.
- 930 https://doi.org/10.1029/2020JE006620
- 931 Romero, C., Sánchez, N., Vegas, J., Galindo, I., 2019. Historic Volcanic Landforms Diversity on
- Lanzarote, in: Mateo, E., Martínez-Frías, J., Vegas, J. (Eds.), Lanzarote and Chinijo Islands
- Geopark: From Earth to Space. Springer International Publishing, Cham, pp. 47–73.
- 934 https://doi.org/10.1007/978-3-030-13130-2 4
- Rowland, S.K., Harris, A.J.L., Garbeil, H., 2004. Effects of Martian conditions on numerically modeled,
- cooling-limited, channelized lava flows. J Geophys Res Planets 109, E10010.
- 937 https://doi.org/10.1029/2004JE002288
- 938 Shahrzad, S., Bramham, E.K., Piazolo, S., Thomas, M., Byrne, P.K., 2024. Amazonian Tectonic
- Evolution of Ceraunius and Tractus Fossae, Mars, and Implications for Local Magmatic Sources.
- J Geophys Res Planets 129, e2023JE008123. https://doi.org/10.1029/2023JE008123
- Taddeucci, J., Alatorre-Ibargüengoitia, M.A., Cruz-Vázquez, O., Del Bello, E., Scarlato, P., Ricci, T.,
- 942 2017. In-flight dynamics of volcanic ballistic projectiles. Reviews of Geophysics 55, 675–718.
- 943 https://doi.org/10.1002/2017RG000564
- Tanaka, K.L., Robbins, S.J., Fortezzo, C.M., Skinner, J.A., Hare, T.M., 2014. The digital global geologic
- map of Mars: Chronostratigraphic ages, topographic and crater morphologic characteristics, and
- 946 updated resurfacing history. Planet Space Sci 95, 11–24. https://doi.org/10.1016/j.pss.2013.03.006
- Thordarson, T., Self, S., 1993. The Laki (Skaftár fires) and Grímsvötn eruptions in 1783–1785. Bull
- 948 Volcanol 55, 233–263.
- 949 Tibaldi, A., Bonali, F.L., Corazzato, C., 2017. Structural control on volcanoes and magma paths from
- local- to orogen-scale: The central Andes case. Tectonophysics 699, 16-41.
- 951 https://doi.org/10.1016/j.tecto.2017.01.005
- Valentine, G.A., Cortés, J.A., Widom, E., Smith, E.I., Rasoazanamparany, C., Johnsen, R., Briner, J.P.,
- Harp, A.G., Turrin, B., 2017. Lunar Crater volcanic field (Reveille and Pancake Ranges, Basin and
- 954 Range Province, Nevada, USA). Geosphere 13, 391–438. https://doi.org/10.1130/GES01428.1
- Vanderkluysen, L., Harris, A.J.L., Kelfoun, K., Bonadonna, C., Ripepe, M., 2012. Bombs behaving
- badly: Unexpected trajectories and cooling of volcanic projectiles. Bull Volcanol 74, 1849–1858.
- 957 https://doi.org/10.1007/s00445-012-0635-8
- Wilson, L., Head, J.W., 1994. Mars: Review and analysis of volcanic erupiton theory and relationships
- to observed landforms. Reviews of Geophysics 32, 221–263. https://doi.org/10.1029/94RG01113

960	Wilson, L., Mouginis-Mark, P.J., Tyson, S., Mackown, J., Garbeil, H., 2009. Fissure eruptions in
961	Tharsis, Mars: Implications for eruption conditions and magma sources. Journal of Volcanology
962	and Geothermal Research 185, 28-46. https://doi.org/10.1016/j.jvolgeores.2009.03.006
963	Wood, C.A., 1979. Monogenetic volcanoes of the terrestial planets, in: 10th Annual Lunar and Planetary
964	Science Conference. pp. 2815–2840.
965	Zarazúa-Carbajal, M.C., Valentine, G.A., De la Cruz-Reyna, S., 2024. Scoria cone erosional degradation
966	by incision: Different behaviors in three volcanic fields reflect environmental conditions. Geology
967	52, 565–569. https://doi.org/10.1130/G52113.1
968	